J. Fluid Mech. (2009), *vol.* 638, *pp.* 199–242. © Cambridge University Press 2009
doi:10.1017/S0022112009990644

Nonlinear interaction between a boundary layer and a liquid film

M. VLACHOMITROU AND N. PELEKASIS†

Department of Mechanical & Industrial Engineering, University of Thessaly, Leoforos Athinon, Pedion Areos, 38834 Volos, Greece

(Received 1 October 2008; revised 1 June 2009; accepted 2 June 2009; first published online 7 October 2009)

The nonlinear stability of a laminar boundary layer that flows at high Reynolds number (Re) above a plane surface covered by a liquid film is investigated. The basic flow is considered to be nearly parallel and the simulations are based on triple deck theory. The overall interaction problem is solved using the finite element methodology with the two-dimensional B-cubic splines as basis functions for the unknowns in the boundary layer and the film and the one-dimensional B-cubic splines as basis functions for the location of the interface. The case of flow above an oscillating solid obstacle is studied and conditions for the onset of Tollmien–Schlichting (TS) waves are recovered in agreement with the literature. The convective and absolute nature of TS and interfacial waves is captured for gas-film interaction, and the results of linear theory are recovered. The evolution of nonlinear disturbances is also examined and the appearance of solitons, spikes and eddy formation is monitored on the interface, depending on the relative magnitude of Froude and Weber numbers (Fr, We), and the gas to film density and viscosity ratios (ρ/ρ_w, μ/μ_w). For viscous films TS waves grow on a much faster time scale than interfacial waves and their effect is essentially decoupled. The influence of interfacial disturbances on short-wave growth in the bulk of the boundary layer bypassing classical TS wave development is captured. For highly viscous films for which inertia effects can be neglected, e.g. aircraft anti-icing fluids, soliton formation is obtained with their height remaining bounded below a certain height. When water films are considered interfacial waves exhibit unlimited local growth that is associated with intense eddy formation and the appearance of finite time singularities in the pressure gradient.

1. Introduction

Boundary layer interaction with solid, liquid or even elastic interfaces manifests itself in a number of technical applications and naturally occurring phenomena. Traditionally, interaction with wall mounted obstacles (Smith 1985; Smith & Bodonyi 1985; Tutty & Cowley 1986), wakes (Veldman 1981) or flow in constricted channels (Smith 1976*a*,*b*; Smith *et al.* 1981) have been studied via steady or unsteady interactive boundary layer calculations in order to examine the effect of wall curvature or wall motion on growth of instabilities and transition. Comparison against experimental observations has shown that such an approach provides very good agreement on account of capturing linear and nonlinear growth of Tollmien–Schlichting (TS) waves and Rayleigh modes, or skin friction and pressure loss in wakes, at large Reynolds

† Email address for correspondence: pel@uth.gr

https://doi.org/10.1017/S0022112009990644 Published online by Cambridge University Press

numbers (Re). Nowadays, direct numerical simulations of the full Navier–Stokes have made such studies just possible without having to resort to the interactive boundary layer formulation.

Nevertheless, recently a wide range of applications have emerged involving boundary layer interaction with a free or an elastic surface. For example, gas–liquid interaction at high Re is of great interest in the study of airfoil performance under rainfall conditions. Experiments that were performed on commercial airfoils by NASA (Bezos *et al.* 1992) have shown that the lift coefficient decreases, whereas the drag increases under such conditions. Experimental measurements with airflow on a wall covered by a viscous liquid film (Ludwieg & Hornung 1989) indicate growth of interfacial waves that may determine transition to turbulence. Steady solutions (Smyrnaios, Pelekasis & Tsamopoulos 2000) for boundary layer flow over a liquid film that grows on a NACA airfoil have indicated upstream movement of the region where flow reversal occurs, with increasing film thickness. Linear stability analysis using the Orr–Sommerfeld equations (Ozgen, Degrez & Sarma 1998) and in the context of triple deck theory (Timoshin 1997; Pelekasis & Tsamopoulos 2001) verifies the importance of interfacial waves, even though their growth rate is lower than that of the TS waves. In particular, it was shown in the latter study that interfacial waves can be absolutely unstable within a parameter range that is relevant to the case of high Re flow above a thin water film. Therefore, it was suggested that the liquid film that covers an airfoil may be responsible for reduction in the lift coefficient, possibly through premature boundary layer separation as a result of their interaction. It is, however, important to ascertain the persistence of the above phenomena in the nonlinear regime.

In the present study, we focus on the stability of a gas boundary layer that interacts with a thin liquid film. The instabilities that appear in such flows are TS waves, interfacial waves and Rayleigh instability. In flows with simple velocity profiles the disturbances that grow faster are TS waves belonging to the lower branch of the neutral stability diagram (Smith 1979*a*). In the context of weakly nonlinear theory (Smith 1979*b*) it was shown that when a boundary layer is perturbed via a periodic excitation that lies beyond the linear stability threshold but sufficiently near criticality, TS waves arise and grow in space until they reach saturation amplitude. When high-frequency disturbances were considered (Smith & Burggraf 1985; Smith 1986) fast growth and spreading was observed without saturation. In fact, the long-time behaviour of initial TS disturbances revealed the possibility for spike formation due to vorticity bursts from the viscous sublayer. Numerical solutions of boundary layer interaction with an oscillating hump that is mounted on a plane wall were performed by Terent'ev (1981, 1984), Ryzhov & Terent'ev (1986) and Duck (1985) using spectral methods verify the results of linear analysis but also capture catastrophic growth of higher modes due to nonlinearity. Furthermore, they indicate growth of Rayleigh modes when the height of the hump exceeds a certain size. Indeed, the appearance of Rayleigh modes and their predominance over TS waves was captured numerically via a finite difference approach by Tutty & Cowley (1986) and verified by linear stability analysis. Rayleigh modes are associated with inflexion points in the basic velocity profile and the onset of flow reversal. TS instabilities are convectively unstable and consequently they tend to travel away from the location of the initial disturbance, while Rayleigh modes lead to eddy splitting and detachment.

Numerical simulations have been extensively used in the past in order to study boundary layer stability and separation via the unsteady interacting boundary layer theory in flow arrangements involving bluff bodies, external vortices, gas–liquid interfaces compliant surfaces and compression ramps. As was mentioned above the

https://doi.org/10.1017/S0022112009990644 Published online by Cambridge University Press

Fourier transform (FT) was employed in some of the earlier studies on the effect of oscillating bodies on boundary layer dynamics, e.g. Terent'ev (1984) and Duck (1985). The bulk of the methods that are available in the literature employ the finite difference method in various contexts.

The alternating direction implicit (ADI) scheme, coupled with a mixed Eulerian–Lagrangian formulation, was employed by Peridier, Smith & Walker (1991*a*,*b*) in order to study vortex induced boundary layer separation over a plane surface in the context of unsteady interacting boundary layer theory. Thus, they were able to capture focusing of the boundary layer into an eruptive spike that leads to separation. They also illustrated numerically that such a behaviour is associated with the formation of a finite time singularity near the surface in the interactive boundary layer formulation. They analysed the dynamics of the singularity and showed that the early stages of its development are in agreement with the theory of Elliott, Cowley & Smith (1983) whereas its final stages evolve towards the structure proposed by Smith (1988) in an article that generalizes the results by Brotherton-Ratcliffe & Smith (1987) on two-fluid flow using triple-deck theory. More specifically, a singularity in the pressure gradient is developed within finite time that is manifested via an eruptive spike in the pressure and displacement thickness profiles. Similar spike formation is observed in the context of the present flow arrangement where the unsteadiness is enforced upon the otherwise steady boundary layer by the film motion. This corroborates the assertion made in the above studies that the process of eruptive spike formation in the interacting boundary layer development is general and not confined to TS waves. In fact, it will be seen here that film viscosity can arrest the evolution of the singularity leading to saturation of the film height and the displacement thickness of the boundary layer. A comprehensive account on the dynamic evolution of spikes and spots in the aftermath of nonlinear TS wave formation and growth, using the two-dimensional and three-dimensional interactive boundary layer formulation, is provided by Smith (1995). More recently, numerical simulations of the two-dimensional Navier–Stokes equations that were performed by Bowles, Davies & Smith (2003) via a hybrid finite difference spectral method, in order to capture nonlinear growth of a TS wavetrain, provided qualitative support of the above described mechanisms for planar boundary layer separation as well as their relevance to the ensuing three dimensional dynamical effects.

In the context of supersonic boundary layers, an implicit first order accurate in time and second-order accurate in space finite difference numerical scheme that was originally developed by Ruban (1978), a similar scheme has also been used by Jenson, Burggraf & Rizzetta (1975), was employed by Cassel, Ruban & Walker (1995, 1996) and more recently by Fletcher, Ruban & Walker (2004) in order to study the onset of absolute and convective instabilities in compression ramp flows. The evolution of unstable wave packets leading to violent breakdown of the boundary layer was discussed in these studies and associated with inflection points in the streamwise velocity component, in the manner pointed out earlier by Tutty & Cowley (1986), while the stabilizing effect of wall cooling was quantified. A more comprehensive list of the available analytical and numerical techniques for solving the unsteady interactive boundary layer formulation is provided by Sychev *et al.* (1998).

The interfacial waves that develop in a gas–liquid interface have smaller growth rates compared to Rayleigh and TS waves (Timoshin 1997; Ozgen *et al.* 1998) and it was shown by linear analysis that they can be either convectively or absolutely unstable (Pelekasis & Tsamopoulos 2001). Linear and nonlinear evolution of travelling waves on a gas–liquid interface was studied by Caponi *et al.* (1982) using a finite difference solution of the two-dimensional Navier–Stokes equations, indicating significant deviations from linear behaviour in the surface-pressure distribution and

https://doi.org/10.1017/S0022112009990644 Published online by Cambridge University Press

wave speed, as the wave steepness increased. These simulations were, however, performed for arbitrary velocity distribution on the interface without proper account of the interaction between the two phases. It will be interesting to verify the extent to which the effects that were identified in the above studies will be recovered in the case of a film interacting with a boundary layer, and the impact that this will have in the exterior flow. In particular the existence of travelling waves for the parameter range that is relevant to realistic gas–liquid systems will be investigated, as is the case with air interacting with a de/anti-icing fluid or water. The evolution of two fluid systems and the development of instabilities and singularities in liquid layers was first studied via the triple-deck formulation by Brotherton-Ratcliffe & Smith (1987). Subsequently, Smith, Li & Wu (2003) studied theoretically the effect of the thin film of air that is formed between a drop and a nearby solid wall as the former impinges on it. Potential flow conditions are assumed in the drop, whereas the formulation in the gas phase ranges from lubrication to unsteady boundary layer or even totally inviscid depending on Reynolds number and the product between viscosity and inverse density ratios. Capillary forces in the air-drop interface were added later by Purvis & Smith (2004) in a study that focused on the delay of drop impact and post impact effect as a result of air cushioning. It will be seen that a similar distinction applies in the present study, in the sense that the viscosity and density ratios between the two fluids determine the validity range of lubrication approximation in the liquid film before film inertia becomes important. The later effect, along with capillarity, plays a central role in the long term dynamics of air-film interaction.

Interaction between a boundary layer and a film is typically treated in the linear limit (Timoshin 1997; Ozgen *et al.* 1998; Pelekasis & Tsamopoulos 2001), with the exception of Tsao, Rothmayer & Ruban (1997) who examined the nonlinear interaction between a boundary layer and a viscous liquid film. In the latter study, agreement between linear theory and numerical simulations was obtained in the range of stable interfacial waves and assuming spatial periodic solutions. Limited results were presented in the unstable regime. The present study is intended to fill this gap by carrying out a numerical investigation that will capture the nonlinear evolution of unstable interfacial waves and their effect on the surrounding boundary layer. To this end, a numerical methodology is developed that not only incorporates the basic features of wave growth, i.e. wavelength, frequency and group velocity, pertaining to the interface and the bulk of the flow, but also captures the effect of nonlinearity on the coupled dynamics between the boundary layer and the film. It is based on the finite element method that accommodates the specific features of such flows as efficiently as possible. As was explained above, triple deck theory provides the theoretical background where all the basic physics of the problem is included. The triple-deck approach conveys the essential information regarding flow-film or flow-obstacle interaction, without, however, the excessive numerical effort that is required by direct numerical simulations (DNS) in order to capture all the relevant time and space scales involved in the two phases. Since the long-time dynamic behaviour of interfacial waves needs to be captured care is taken to optimize the accuracy of the method while eliminating growth of unwanted short waves. Therefore, motivated by the encouraging results from studies on interfacial instabilities of oscillating bubbles (Pelekasis, Tsamopoulos & Manolis 1992), we introduce two-dimensional B-cubic splines as basis functions (Prender 1989) and compare their performance against the standard biquadratic Lagrangian basis functions.

In § 2 the governing equations for flow over a liquid film or a moving solid obstacle are presented. The numerical method that was developed specifically for this type

https://doi.org/10.1017/S0022112009990644 Published online by Cambridge University Press

of problems is described in detail in § 3. The reliability of the numerical method is tested by solving the flow of air above a moving hump that is mounted on a flat plate, in order to capture TS waves and eddy formation and compare against existing numerical–theoretical studies. Finally, in § 4 we present the results and conclusions that were drawn based on the simulations for boundary layer interaction with a liquid film. In § 4.1 numerical results for the development of TS and interfacial waves are presented, in which case it is shown that gas flow is essentially quasi-steady on the time scale of interfacial waves for films with much larger viscosity in comparison with that of air, e.g. water or de/anti-icing fluid. In § 4.2 emphasis is placed on the evolution of interfacial waves for films of this type. The appearance of travelling waves and solitons is investigated as well as the case of absolute versus convective instability. The results are classified parametrically in terms of the Froude and Weber numbers as well as parameter $\mathfrak{M}$ which is associated with the gas to film viscosity (μ/μ_w) and density (ρ/ρ_w) ratios and is a measure of film inertia. The appearance of singularities in the flow pattern is addressed in the context of previous theoretical predictions and their effect in boundary layer separation is discussed. Finally, the main conclusions of our investigation are presented in § 5.

2. Problem formulation

2.1. *Basic flow*

We consider a thin liquid film of density ρ_w and viscosity μ_w that covers a flat plate of characteristic length L. Above the film flows a gas stream of density ρ, viscosity μ and free stream velocity U_∞, $Re = U_\infty \rho L/\mu \gg 1$, that puts the film into motion. The equations that describe the basic flow have been calculated numerically as well as asymptotically (Nelson, Alving & Joseph 1995; Smyrnaios *et al.* 2000). In the limit $\varepsilon = H_f/(L\,Re^{-1/2}) \to 0$, where H_f is the film thickness and $LRe^{-1/2}$ the thickness of the boundary layer, the solution inside the boundary layer assumes the Blasius profile U_O. The shear stress inside the boundary layer is $\partial U_0/\partial Y'(x, Y' = 0) = 0.332/\sqrt{x}$ where $Y' = LRe^{-1/2}$. Inside the liquid film the thickness and the velocity are

$$H_o(x) = x^{3/4}\sqrt{\frac{2}{0.332}}; \quad u_o(x, y) = x^{1/4} z\sqrt{0.664}, \quad z = \frac{y}{H_0(x)}; \tag{2.1a}$$

$$H_o(x) = x^{1/4}\sqrt{\frac{2}{0.332}}; \quad u_o(x, y) = x^{-1/4} z\sqrt{0.664}, \quad z = \frac{y}{H_0(x)}; \tag{2.1b}$$

when a constant rainfall (Smyrnaios *et al.* 2000) or constant mass flow rate (Timoshin 1997; Nelson *et al.* 1995) is assumed, respectively. The characteristic scales that have been used in the gas phase are L, $LRe^{-1/2}$ as characteristic length scales in the x and y directions, respectively, and U_∞, $U_\infty Re^{-1/2}$ as characteristic velocities in the x and y directions, respectively. In the liquid film L, H_f have been used as characteristic length scales in x and y directions, and u_f, $u_f H_f/L$ as characteristic velocities in the x and y directions, respectively. Relevant estimates of H_f and u_f are provided by Smyrnaios *et al.* (2000) and Nelson *et al.* (1995) for the case of a steady rainfall rate $\dot{r}$ and constant mass flow rate Q, respectively, based on the mass and shear stress balances written on the gas–liquid interface.

2.2. *Governing equations*

We are interested in examining the nonlinear stability of two-dimensional laminar airflow past a solid obstacle mounted on an otherwise flat plate or a thin liquid film

https://doi.org/10.1017/S0022112009990644 Published online by Cambridge University Press

that develops on a flat plate. We consider a flat plate of characteristic length L and a gas stream that flows at high Re above this plate.

It is widely accepted that the appropriate asymptotic framework to study the stability of a boundary layer in the presence of an obstacle, in the limit of large Re numbers, is provided by triple deck theory (Smith *et al.* 1981). It provides a starting point for establishing conditions for which the dynamics of an interface can possibly trigger dramatic changes, such as flow reversal or massive separation in the boundary layer. For an external flow characterized by a free stream velocity U_∞ that flows over a surface whose length scale is L, as $Re = U_\infty L/\nu$ asymptotically increases the thickness of the internal viscous sublayer $O(Re^{-5/8}L)$ is determined by the requirement that the inertia and viscous contributions of the disturbance flow field balance each other. The length of the viscous sublayer $O(Re^{-3/8}L)$ is determined by the requirement that changes in the pressure inside the viscous sublayer can interact with and affect pressure variations of the outer flow. Thus, the axial velocity is scaled by velocity gradients in the transverse direction as viewed inside the sublayer $(U_\infty/LRe^{-1/2})LRe^{-5/8} \approx U_\infty Re^{-1/8}$. The middle layer thickness is the same as the classical boundary layer thickness $O(Re^{-1/2})$, whereas that of the external layer is the same as the length scale in the axial direction $O(Re^{-3/8})$.

The fastest growing disturbances in boundary layer flow correspond to wavelengths belonging to the range of length scales of the triple deck theory (Smith 1979*a*). In this context, the appropriate local scale to describe the stability of the flow at a given position $x = x_o$ is $X = (x - x_0)/\lambda$, where $\lambda = Re^{-3/8}L$. Clearly, the local scale $X \sim \lambda = LRe^{-3/8}$ is much smaller than the scale of the basic flow $x \sim L$. Therefore the basic flow can be considered to be nearly parallel as far as the development of instabilities is concerned. The shortest obstacle that can cause flow separation has comparable thickness with the viscous sublayer in the gas phase $H_f \sim Re^{-5/8}L$. Subsequently, dimensionless quantities are introduced via the following characteristic scales: length $\lambda = LRe^{-3/8}$ in the streamwise direction and thickness $LRe^{-5/8}$ in the perpendicular direction for both the gas stream and the film/obstacle. The film thickness as estimated by the base flow (Smyrnaios *et al.* 2000; Nelson *et al.* 1995) is indeed on the order $H_f = LRe^{-5/8}$. The characteristic velocities in the gas phase are εU_∞ in the streamwise direction and $\varepsilon^3 U_\infty$ in the perpendicular one, $\varepsilon = Re^{-1/8}$, whereas in the liquid phase the characteristic velocities are $u_f = (\mu/\mu_w)\varepsilon U_\infty$ and $(\mu/\mu_w)\varepsilon^3 U_\infty$ in the streamwise and perpendicular directions, respectively. In the following μ and ρ denote viscosity and density whereas subscript w signifies properties of the film. Quantity $\varepsilon^2 \rho U_\infty^2$ is used as a pressure scale for both phases. The above scales are obtained as a result from balancing the inertia, viscous and pressure terms. The small term in the asymptotic description of the triple deck theory is equal to $\varepsilon = H_f/LRe^{-1/2} = Re^{-1/8}$. Finally, the appropriate time scales are $t = \lambda/\varepsilon U_\infty$ for TS waves and $T = \lambda/u_f = \lambda/\varepsilon(\mu/\mu_w)U_\infty$ for interfacial waves. Since we are interested in the effect of interfacial waves on the boundary layer we chose the time scale furnished by the motion of the interface in the dimensionless formulation that follows.

We obtain the dimensionless problem formulation in the context of nonlinear triple deck theory, following previous studies on boundary layer stability (Smith 1979*a*, *b*; Timoshin 1997; Pelekasis & Tsamopoulos 2001) upon introduction of the characteristic scales listed in the previous paragraph. In the gas phase we use the transformed variable $\overline{Y} = Y - H(X, t)$, where H is the dimensionless film thickness. Moreover, we introduce Prandtl's transposition via variable $\overline{V}$, where $\overline{V} = V - U(\partial H/\partial X) - (\mu/\mu_w)(\partial H/\partial T)$. Therefore the dimensionless equations that describe the flow in the viscous sublayer of the boundary layer are

https://doi.org/10.1017/S0022112009990644 Published online by Cambridge University Press

X-momentum:

$$\frac{\mu}{\mu_w}\frac{\partial U}{\partial T}+U\frac{\partial U}{\partial X}-\frac{\partial \Psi}{\partial X}\frac{\partial U}{\partial \overline{Y}}=-\frac{\partial P}{\partial X}+\frac{\partial^2 U}{\partial \overline{Y}^2},\quad U=\frac{\partial \Psi}{\partial \overline{Y}},\tag{2.2a,b}$$

with ψ the streamfunction. Y-momentum establishes the pressure as being independent from the transverse direction

$$\frac{\partial P}{\partial \overline{Y}}=0.\tag{2.3}$$

The pressure is related to the displacement thickness through the interaction law, which arises from the solution of Laplace's equation in the upper deck of the boundary layer:

$$P=\frac{1}{\pi}\int_{-\infty}^{+\infty}\frac{\partial A}{\partial s}\frac{\mathrm{d}s}{X-s}.\tag{2.4}$$

The velocity has to match as the viscous sublayer merges with the main deck. Therefore,

$$U(\overline{Y}\to\infty)=\frac{\partial U_0}{\partial Y'}(x_0,Y'=0)\left(A(X)+\overline{Y}+H-H_0+\frac{\mu}{\mu_w}H_0\right),\tag{2.5}$$

where $\partial U_0/\partial Y'(x,Y'=0)$ and H_0 refer to the shear stress on the flat plate and the film thickness as predicted by the base solution U_0 in the gas stream. U_0 is the Blasius solution with $Y=LRe^{-1/2}$. When the displacement thickness vanishes, $A=0$, the velocity of the gas stream, evaluated on the gas-film interface for the base flow, is recovered. In the liquid film we introduce the transformed variable $\overline{\overline{y}}=y/H(X,t)$ along with the triple-deck length and time scales. Thus, conditions on the gas–liquid interface, $\bar{Y}=0$, $\overline{\overline{y}}=1$, read:

continuity of tangential and normal velocities:

$$U=\frac{\mu}{\mu_w}u,\quad \left.\frac{\partial \Psi}{\partial X}\right|_{\overline{Y}=0}=0,\tag{2.6a,b}$$

continuity of tangential and normal stresses:

$$\frac{\partial U}{\partial \overline{Y}}=\frac{1}{H}\frac{\partial u}{\partial \overline{\overline{y}}},\quad P-p=\frac{1}{\overline{\overline{We}}}\frac{\partial^2 H}{\partial X^2}\tag{2.7a,b}$$

and the kinematic boundary condition:

$$\frac{\partial H}{\partial T}+\frac{\partial \psi}{\partial X}=0;\tag{2.8}$$

capital and small case letters denote quantities defined in the gas phase and the film, respectively.

In the x-momentum inside the film we substitute the normal force balance, equation (2.7*b*), for the liquid pressure. Thus, the governing equations in the film are

X-momentum:

$$\mathfrak{M}\left(\frac{\partial u}{\partial T}+u\frac{\partial u}{\partial X}+\frac{\overline{\overline{y}}-1}{H}\frac{\partial u}{\partial \overline{\overline{y}}}\frac{\partial \psi}{\partial X}\right)=-\frac{\partial P}{\partial X}+\frac{1}{\overline{\overline{We}}}\frac{\partial^3 H}{\partial X^3}-\frac{\left(\frac{\rho_w}{\rho}-1\right)}{\overline{Fr}}\frac{\partial H}{\partial X}+\frac{1}{H^2}\frac{\partial^2 u}{\partial \overline{\overline{y}}^2},\quad u=\frac{1}{H}\frac{\partial \psi}{\partial \overline{\overline{y}}},\tag{2.9a,b}$$

https://doi.org/10.1017/S0022112009990644 Published online by Cambridge University Press

where ψ is the stream function in the film and $v = -\left.\frac{\partial \psi}{\partial X}\right|_{\overline{\overline{y}}}$,

y-momentum:

$$\frac{\partial p}{\partial \overline{\overline{y}}} = 0 \tag{2.10}$$

and the non-slip non-penetration conditions on the surface of the flat plate:

$$\overline{\overline{y}} = 0: \quad u = \psi = 0; \tag{2.11}$$

coefficient $\left(\overline{\overline{y}} - 1\right)/H$ in (2.9) arises from the variable transformation in the y direction in the liquid film which yields

$$\left.\frac{\partial u}{\partial T}\right|_{X,y} = \left.\frac{\partial u}{\partial T}\right|_{X,\overline{\overline{y}}} - \frac{\overline{\overline{y}}}{H}\frac{\partial \psi}{\partial \overline{\overline{y}}}\frac{\partial H}{\partial T} = \left.\frac{\partial u}{\partial T}\right|_{X,\overline{\overline{y}}} + \frac{\overline{\overline{y}}}{H}\frac{\partial \psi}{\partial \overline{\overline{y}}}\frac{\partial \psi}{\partial X}$$

and

$$\left.\frac{\partial \psi}{\partial X}\right|_{X,y} = \left.\frac{\partial \psi}{\partial X}\right|_{X,\overline{\overline{y}}} - \frac{\overline{\overline{y}}}{H}\frac{\partial \psi}{\partial \overline{\overline{y}}}\frac{\partial H}{\partial X}.$$

In the above formulation dimensionless parameters arise that determine the importance of inertia, surface tension and gravitational forces, respectively, in the film motion,

$$\mathfrak{M} = \left(\frac{\mu}{\mu_w}\right)^2 \frac{\rho_w}{\rho}, \frac{1}{\overline{We}} = \left(\frac{\mu}{\mu_w}\right)^2 \frac{1}{We} = \left(\frac{\mu}{\mu_w}\right)^2 \frac{\varepsilon^4 \sigma}{\rho u_f^2 H_f}$$

and

$$\frac{1}{\overline{\overline{Fr}}} = \left(\frac{\mu}{\mu_w}\right)^2 \frac{1}{Fr} = \left(\frac{\mu}{\mu_w}\right)^2 \frac{g H_f}{u_f^2}.$$

$\overline{We}$ and $\overline{Fr}$ denote modified Weber and Froude numbers that incorporate the air/film viscosity ratio in such a way as to become, roughly, $O(1)$ quantities. Finally, $\partial U_0/\partial Y'(x_0, Y' = 0) = 0.332/\sqrt{x_0}$ and H_0 contain information regarding the base flow at the point of inception of the disturbance, x_0. When the film viscosity is much larger than the viscosity of the gas, $\mu/\mu_w \to 0$, interfacial waves evolve on a much slower time scale than TS waves (Pelekasis & Tsamopoulos 2001; Rothmayer, Matheis & Timoshin 2002). Since the time scale relevant to the evolution of interfacial waves is employed for rendering time dimensionless, the small parameter μ/μ_w appears in the transient term of (2.2a). When the evolution of interfacial waves is of interest the transient term can be dropped from the equations of motion in the gas phase which is assumed to be in a quasi-steady state, after an initial transient has elapsed, whereby the film imposes its dynamics on the gas stream via changes in the film height. Along with the transient term that is dropped out of the X-momentum (defined in (2.2)), the tangential and normal velocities (defined in (2.6)) are also taken to vanish at the interface. In this fashion the spatiotemporal evolution of the interfacial waves can be investigated decoupled from the TS waves. Interaction between a boundary layer of air and a growing water film falls in this category. In the special case where $\mathfrak{M} \to 0$ the resulting equation that describes flow in the liquid film does not include inertia terms, thus providing the spatiotemporal evolution of the interface as a result

https://doi.org/10.1017/S0022112009990644 Published online by Cambridge University Press

of shear, pressure, surface tension and gravity forces:

$$\frac{\partial H}{\partial T} = -\frac{\partial}{\partial X}\left(\frac{H^2}{2}\left.\frac{\partial U}{\partial \overline{Y}}\right|_{\bar{Y}=0}\right) + \frac{\partial}{\partial X}\left(\frac{H^3}{3}\frac{\partial P}{\partial X}\right) - \frac{\partial}{\partial X}\left(\frac{H^3}{3\overline{We}}\frac{\partial^3 H}{\partial X^3}\right) + \frac{\partial}{\partial X}\left(\frac{H^3}{3}\frac{(\rho_w/\rho - 1)}{\overline{Fr}}\frac{\partial H}{\partial X}\right). \quad (2.12)$$

The above equation is derived by solving the X momentum in the film for the streamwise velocity U, after eliminating inertia terms and incorporating the interfacial and boundary conditions. It pertains mostly to the interaction of anti-icing fluids with an oncoming boundary layer of air, owing to the very large viscosity of the former.

In the context of the present study three different problems are solved. The first one corresponds to the overall study of growth of interfacial waves in the presence of TS waves and comprises (2.2) and (2.9), subject to conditions (2.3)–(2.7), (2.10) and (2.11) and kinematic condition (2.8). The second and third problems assume a quasi-steady state inside the gas phase and concentrate solely in the study of interfacial waves on films that are much more viscous than the gas stream. Consequently, the temporal term in (2.2) is omitted. When film inertia is important based on parameter $\mathfrak{M}$, e.g. water films, (2.9) describes film motion, whereas for flow of films with negligible inertia, e.g. many deicing fluids, the lubrication type formulation provided by (2.12) is employed inside the film. The relevance of the product between viscosity and inverse density ratio in obtaining the appropriate formulation inside a thin film, lubrication versus unsteady boundary layer, has also been pointed out by Smith *et al.* (2003) in their study of the air cushioning effect during drop impact on a solid wall. In the latter study it is the air that forms a film which impedes drop impact.

In all cases we perturb the basic solution by introducing a disturbance either on the interface or on the streamwise velocity in the bulk of the boundary layer:

$$H(T=0) = H_0(T=0) + H_D,\ U(T=0, X, \overline{Y}) = U_0(X, \overline{Y}) + U_D, \quad (2.13)$$

where H_D and U_D denote the imposed disturbance which can be either instantaneous or periodic:

$$H_D = d\sqrt{\frac{W}{\pi}}\exp(-WX^2), \quad H_D = d\sqrt{\frac{W}{\pi}}\exp(-WX^2)\cos(\omega T), \quad (2.14a,b)$$

where d corresponds to the magnitude of the disturbance, W defines its range in the streamwise direction and ω is the dimensionless frequency of the disturbance; W is set to 4 in the simulations conducted herein. A similar disturbance is used for the streamwise velocity located at a certain $\bar{Y}$ location in the boundary layer.

3. Numerical solution

In order to investigate the flow configurations described above, it is crucial to develop a numerical approach that provides accurate results while at the same time minimizes the requirements for storage and processing time. The numerical schemes that are available in the literature employ finite difference (Jenson *et al.* 1975; Ruban, 1978; Veldman 1981; Tutty & Cowley 1986; Peridier *et al.* 1991*a*,*b*; Cassel *et al.* 1995, 1996; Tsao *et al.* 1997; Fletcher 2004), spectral methods (Terent'ev 1981, 1984; Duck 1985) or a combination of the two methods for the solution of the nonlinear triple-deck equations for incompressible and compressible flow arrangements. In the present study the finite element method is adopted owing to its better flexibility in capturing moving

https://doi.org/10.1017/S0022112009990644 Published online by Cambridge University Press

interfaces under quite intense shape variations. Especially when steep waveforms arise, as will be seen to be the case here, the finite element methodology is expected to behave better than spectral or finite difference techniques (Gresho & Sani 1998). In the finite element methodology the basis functions play a central role in optimizing accuracy of the results. Recently, the development of high-order polynomial basis functions has received a significant amount of attention as an alternative to the traditional quadratic Lagrangian polynomials. Cubic and bicubic B-splines have been used in order to interpolate the unknown shape of an interface in the framework of boundary integral methodology. Their increased smoothness and accuracy characteristics provided very reliable representations of the interface for prolonged time integration under severe external disturbances.

3.1. *Finite element methodology*

We compared the biquadratic Lagrangian and bicubic *B*-splines, in terms of their efficiency as basis functions of the finite element representation of the flow under examination. It is known that the quadratic Lagrangian basis functions are polynomials of second order, while cubic *B*-splines are polynomials of third order. Interpolations of unknown functions in terms of the former basis functions only guarantee continuity of the interpolating function whereas the latter allow for continuous first and second derivatives (Prender 1989). In either case the local two-dimensional basis functions corresponding to rectangular elements, arise as a result of tensorial multiplication of the one-dimensional functions in x and y direction:

$$N_k(x, y) = L_i(x)L_j(y) \quad k = 1, 2 \ldots 9, \quad i, j = 1, 2, 3, \tag{3.1}$$

$$N_k(x, y) = B_i(x)B_j(y), \quad k = 1, 2 \ldots 16, \quad i, j = 1, 2, 3, 4, \tag{3.2}$$

$$\begin{aligned} L_1(x) &= \frac{(2x - x_{i+1} - x_i)(2x - 2x_{i+1})}{2h^2}, \quad L_2(x) = \frac{(2x - 2x_i)(2x_{i+1} - 2x)}{h^2}, \\ L_3(x) &= \frac{(2x - x_{i+1} - x_i)(2x - 2x_i)}{2h^2}, \quad x \in [x_i, x_{i+!}], \quad h = x_{i+1} - x_i, \end{aligned} \tag{3.3}$$

$$B_i(x_j) = \frac{1}{h^3} \begin{cases} (x - x_{i-2})^3, & x \in [x_{i-2}, x_{i-1}] \\ h^3 + 3h^2(x - x_{i-1}) + 3h(x - x_{i-1})^2 - 3(x - x_{i-1})^3, & x \in [x_{i-1}, x_i] \\ h^3 + 3h^2(x_{i+1} - x) + 3h(x_{i+1} - x)^2 & \\ \quad -3(x_{i+1} - x)^3, & x \in [x_i, x_{i+1}] \quad h = x_{i+1} - x_i, \\ (x_{i+2} - x)^3, & x \in [x_{i+1}, x_{i+2}] \\ 0, & x \notin [x_{i-2}, x_{i+2}] \end{cases} \tag{3.4}$$

where L_i, B_i denote the local one-dimensional Lagrangian and *B*-spline basis functions, respectively, and N_k the local two-dimensional ones. Equation (3.4) applies for a uniform mesh. Clearly the B_i's so defined are twice continuously differentiable, i.e. C^2 continuous. It can also be shown (De Boor 1978) that they are the cubic splines with the smallest compact support, each of them is non-zero over four consecutive elements, satisfying C^2 continuity. As is well known, the Lagrangian basis functions satisfy C^0 continuity with smaller compact support, i.e. they extend over two consecutive elements. In figures 1(*a*) and 1(*b*) a schematic representation of one-dimensional and two-dimensional cubic *B*-splines is provided for the case of uniform element size. Derivation of the cubic *B*-splines corresponding to varying element size distribution is tedious but straightforward (De Boor 1978), hence it is not provided here. With the Lagrangian biquadratic basis functions the interpolate $\bar{f}$ of a function f on a domain that is discretized via a certain sequence of nodes x_j is obtained in

https://doi.org/10.1017/S0022112009990644 Published online by Cambridge University Press

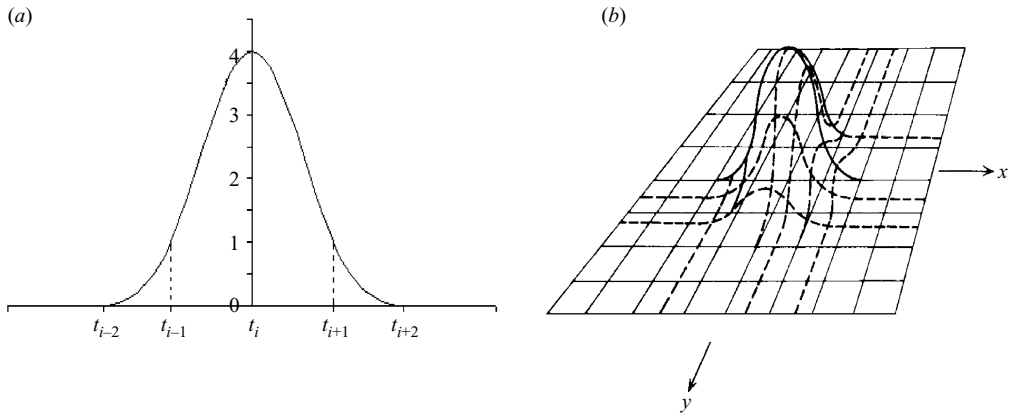


FIGURE 1. Schematic representation of B-cubic splines in (*a*) one-dimensional and (*b*) two-dimensional; adapted from Prender (1989).

terms of a summation over the products between the function values at the nodes and the global basis functions that are centred on the specific nodes

$$\bar{f}(x) = \sum_{i=1}^{2n+1} c_i \Lambda_i(x) \quad \text{for } n \text{ quadratic elements}, \tag{3.5}$$

where c_i and $\Lambda_i(x)$ denote the function values at the $2n+1$ nodes and the global quadratic basis functions satisfying $\Lambda_i(x_j) = \delta_{ij} \quad i, j = 1, 2, 3 \ldots 2n+1$, where δ represents the Kronecker delta. When the cubic *B*-splines are employed over the same number of elements the interpolate assumes the form

$$\bar{f}(x) = \sum_{i=0}^{n+2} c_i \Lambda_i(x) \quad \text{for } n \text{ elements}. \tag{3.6}$$

Now the coefficients c_i are dissociated from the function values, being coefficients of the spline representation. Two additional coefficients are introduced, c_0 and c_{n+2}, corresponding to two fictitious nodes each located immediately before and after the interpolation region (x_1, x_{n+1}). They are essential in order to satisfy the continuity requirements of the interpolate function. Four global basis functions survive locally within each element $[x_i, x_{i+1}]$ while three such functions are required to obtain the interpolation at node x_i, as opposed to three local quadratic basis functions within one element. In order to calculate the unknown coefficients c_i of the spline representation (3.6) two additional conditions are needed, normally setting the first or second derivative of the interpolated function at the boundaries of the domain (Prender 1989) to a specific value. As long as the interpolated function is sufficiently differentiable the quadratic and cubic *B*-spline representations provide $O(h^3)$ and $O(h^4)$ accurate interpolates; h denotes a measure of the element size. These ideas can be extended to two dimensions in which case the interpolate function reads

$$\bar{f}(x, y) = \sum_{i=1}^{n+1} \sum_{j=1}^{m+1} c_{ij} M_{ij}(x, y) \quad \bar{f}(x, y) = \sum_{i=0}^{n+2} \sum_{j=0}^{m+2} c_{ij} M_{ij}(x, y) \tag{3.7}$$

https://doi.org/10.1017/S0022112009990644 Published online by Cambridge University Press

for $n \times m$ biquadratic and bicubic B-spline elements, respectively, with M_{ij} the global two-dimensional basis functions in either case. Within each element nine local biquadratic and sixteen local bicubic B-spline basis functions survive, while on a certain node a single coefficient is required for interpolating a function with the biquadratic representation versus a summation over nine neighbouring coefficients for the bicubic B-spline representation. Thus, the weak formulation of the problem as described via (2.2*a*,*b*) and (2.9*a*,*b*) reads

$$\int_0^{\bar{Y}_{inf}}\int_{-X_1}^{X_2} M_{ij}\left(\frac{\mu}{\mu_w}\frac{\partial U}{\partial t}+U\frac{\partial U}{\partial X}-\frac{\partial \Psi}{\partial X}\frac{\partial U}{\partial \overline{\bar{Y}}}\right)\mathrm{d}X\ \mathrm{d}\bar{Y}-\int_0^{\bar{Y}_{inf}}\int_{-X_1}^{X_2}\frac{\partial M_{ij}}{\partial X}P\ \mathrm{d}X\ \mathrm{d}\bar{Y}$$
$$+\int_0^{\bar{Y}_{inf}}\int_{-X_1}^{X_2}\frac{\partial M_{ij}}{\partial \overline{\bar{Y}}}\frac{\partial U}{\partial \overline{\bar{Y}}}\ \mathrm{d}X\ \mathrm{d}\overline{\bar{Y}}+\int_0^{\bar{Y}_{inf}} M_{ij}(P_{x_0}-P_{-x_0})\ \mathrm{d}\bar{Y}$$
$$-\int_{-X_1}^{X_2} M_{ij}\left(\left.\frac{\partial U}{\partial \overline{\bar{Y}}}\right|_{\bar{Y}=\bar{Y}_{inf}}-\left.\frac{\partial U}{\partial \overline{\bar{Y}}}\right|_{\bar{Y}=0}\right)\mathrm{d}X=0, \tag{3.8a}$$

$$\int_0^{\bar{Y}_{inf}}\int_{-X_1}^{X_2} M_{ij}U(X,\bar{Y})\ \mathrm{d}X\ \mathrm{d}\bar{Y}=\int_0^{\bar{Y}_{inf}}\int_{-X_1}^{X_2} M_{ij}\frac{\partial \Psi}{\partial \overline{\bar{Y}}}(X,\bar{Y})\ \mathrm{d}X\ \mathrm{d}\bar{Y}, \tag{3.8b}$$

$$\int_0^{1}\int_{-x_1}^{x_2} M_{ij}\left(\frac{\partial u}{\partial t}+u\frac{\partial u}{\partial X}+\frac{\overline{\bar{y}}-1}{H}\frac{\partial \psi}{\partial X}\frac{\partial u}{\partial \overline{\bar{y}}}\right)\mathrm{d}X\ \mathrm{d}\overline{\bar{y}}-\int_0^{1}\int_{-x_1}^{x_2}\frac{\partial M_{ij}}{\partial X}P\ \mathrm{d}X\ \mathrm{d}\overline{\bar{y}}$$
$$+\int_0^{1}\int_{-X_1}^{X_2}\frac{\partial M_{ij}}{\partial X}\frac{1}{\overline{We}}\frac{\partial^2 H}{\partial X^2}\ \mathrm{d}X\ \mathrm{d}\overline{\bar{y}}+\int_0^{1}\int_{-X_1}^{X_2}\frac{\partial M_{ij}}{\partial X}\frac{(\rho_w/\rho-1)}{\overline{Fr}}\frac{\partial H}{\partial X}\ \mathrm{d}X\ \mathrm{d}\overline{\bar{y}}$$
$$+\int_0^{1}\int_{-X_1}^{X_2}\frac{\partial M_{ij}}{\partial \overline{\bar{y}}}\frac{1}{H^2}\frac{\partial u}{\partial \overline{\bar{y}}}\ \mathrm{d}X\ \mathrm{d}\overline{\bar{y}}+\int_0^{1} M_{ij}(P_{x_0}-P_{-x_0})\,\mathrm{d}\overline{\bar{y}}-\int_0^{1} M_{ij}\frac{1}{\overline{We}}\left(\left.\frac{\partial^2 H}{\partial X^2}\right|_{x_0}\right.$$
$$\left.-\left.\frac{\partial^2 H}{\partial X^2}\right|_{-x_0}\right)\mathrm{d}\overline{\bar{y}}-\int_{-X_1}^{X_2} M_{ij}\frac{1}{H^2}\left(\left.\frac{\partial u}{\partial \overline{\bar{y}}}\right|_{\overline{\bar{y}}=1}-\left.\frac{\partial u}{\partial \overline{\bar{y}}}\right|_{\overline{\bar{y}}=0}\right)\mathrm{d}X=0, \tag{3.9a}$$

$$\int_0^{1}\int_{-X_1}^{X_2} M_{ij}u(X,\overline{\bar{y}})\ \mathrm{d}X\ \mathrm{d}\overline{\bar{y}}=\int_0^{1}\int_{-X_1}^{X_2} M_{ij}\frac{1}{H(X,t)}\frac{\partial \psi}{\partial \overline{\bar{y}}}(X,\overline{\bar{y}})\ \mathrm{d}X\ \mathrm{d}\overline{\bar{y}} \tag{3.9b}$$

in the gas and liquid phase, respectively. In the following k denotes the total number of nodes in the domain discretization consisting of n by m elements in the x and y directions; $k=(2n+1)(2m+1)$ for biquadratic Lagrangian and $(n+3)(m+3)$ for bicubic B-splines, respectively. All the unknown functions are approximated in the

https://doi.org/10.1017/S0022112009990644 Published online by Cambridge University Press

standard finite element fashion:

$$U\left(X,\overline{\bar{y}},t\right)=\sum_{i=1}^{k}a_i(t)M_{ij}\left(X,\bar{Y}\right),\quad \Psi\left(X,\bar{Y},t\right)=\sum_{i=1}^{k}b_i(t)M_{ij}\left(X,\bar{Y}\right),$$
$$u\left(X,\overline{\bar{y}},t\right)=\sum_{i=1}^{k}c_i(t)M_{ij}\left(X,\overline{\bar{y}}\right),\quad \psi\left(X,\overline{\bar{y}},t\right)=\sum_{i=1}^{k}d_i(t)M_{ij}\left(X,\overline{\bar{y}}\right),$$
$$P(X,t)=\sum_{i=1}^{n}e_i(t)\Lambda_i(X),\quad A(X),t=\sum_{i=1}^{n}f_i(t)\Lambda_i(X),\quad H(X,t)=\sum_{i=1}^{n}g_i(t)\Lambda_i(X). \tag{3.10}$$

It should be noted that a staggered mesh is not required for the pressure in this case since it is not associated with the constraint of mass continuity. The pressure is evaluated via the integral equation (2.4) involving the displacement thickness. The latter is discretized in the X direction and evaluated using Gaussian integration with X running from $-X_1$ to X_2, for the pressure values at a certain X_i position. The singularity at $X_i=s$ is thus removed as s approaches X_i from left and right (Veldman 1981). The far field condition where the lower and middle decks merge (defined in (2.5)) provides the boundary condition for the longitudinal velocity in the gas phase as well as an extra condition setting the displacement thickness. Finally, the kinematic condition (2.8) is employed in order to solve for the location of the interface. It is discretized using the finite element methodology

$$\int_{-X_0}^{X_0}\Lambda_i(X)\frac{\partial H}{\partial t}\,\mathrm{d}X+\int_{-X_0}^{X_0}\Lambda_i(X)\frac{\partial \psi}{\partial X}\,\mathrm{d}X=0; \tag{3.11}$$

$i=1,2\ldots 2n+1$ for n biquadratic and $i=1,2\ldots n+3$ for n bicubic elements.

Continuity of the longitudinal and normal velocities as well as the shear stress at the interface (defined in (2.6*a*,*b*) and (2.7*a*)) are employed in order to connect the velocity field in the two phases, while continuity of the normal stress is used in order to eliminate liquid pressure. The non-slip non-penetration conditions (2.11) are imposed on the flat plate.

The same procedure is applied when the film viscosity is much larger than the viscosity of the gas, $\mu/\mu_w\to 0$. The only difference is that a quasi-steady state is assumed in the gas phase and as a consequence the local acceleration term is dropped out of (3.8*a*). Finally, in the special case where $\mathfrak{M}\to 0$, we introduce the one-dimensional basis functions and thus the weak formulation of (2.12) assumes the form:

$$\int_{-x0}^{x0}\Lambda_i\frac{\mathrm{d}H}{\mathrm{d}t}\,\mathrm{d}X=\int_{-x0}^{x0}\left(\frac{\mathrm{d}\Lambda_i}{\mathrm{d}X}\frac{H^2}{2}\frac{\partial U}{\partial\overline{\bar{Y}}}-\frac{\mathrm{d}\Lambda_i}{\mathrm{d}X}\frac{H^3}{3}\frac{\partial P}{\partial X}\right)\mathrm{d}X-\int_{-x0}^{x0}\left(\frac{\mathrm{d}^2\Lambda_i}{\mathrm{d}X^2}\frac{H^3}{3\overline{We}}\frac{\partial^2 H}{\partial X^2}\right)\mathrm{d}X$$
$$-\int_{-x0}^{x0}\left(\frac{\mathrm{d}\Lambda_i}{\mathrm{d}X}\frac{H^2}{\overline{We}}\frac{\partial H}{\partial X}\frac{\partial^2 H}{\partial X^2}-\frac{\mathrm{d}\Lambda_i}{\mathrm{d}X}\frac{H^3}{3}\frac{\rho_w/\rho-1}{Fr}\frac{\partial H}{\partial X}\right)\mathrm{d}X+\left[\frac{\mathrm{d}\Lambda_i}{\mathrm{d}X}\frac{H^3}{3\overline{We}}\frac{\partial^2 H}{\partial X^2}\right]_{-x0}^{x0}$$
$$-\left[\Lambda_i\frac{H^2}{2}\frac{\partial U}{\partial\overline{\bar{Y}}}\right]_{-x0}^{x0}+\left[\Lambda_i\frac{H^3}{3}\frac{\partial P}{\partial X}\right]_{-x0}^{x0}-\left[\Lambda_i\frac{H^3}{3\overline{We}}\frac{\partial^3 H}{\partial X^3}\right]_{-x0}^{x0}+\left[\Lambda_i\frac{H^3}{3}\frac{\rho_w/\rho-1}{Fr}\frac{\partial H}{\partial X}\right]_{-x0}^{x0}, \tag{3.12}$$

where $i=1,2\ldots 2n+1$ for n quadratic and $i=1,2\ldots n+3$ for n cubic elements.

https://doi.org/10.1017/S0022112009990644 Published online by Cambridge University Press

3.2. *Time integration*

The fourth-order Runge–Kutta (RK) time integrator and the trapezoidal rule were employed for the discretization of time derivatives. The former approach is explicit and consequently resulted in relatively small time steps in order to maintain numerical stability. The additional requirement of the RK method for internal time steps, accompanied by upgrades of the system matrix to be inverted, further intensifies the computational load. Consequently the trapezoidal rule was selected as the optimal choice for time integration. The fact that it is less accurate than the RK method does not affect the overall accuracy of the solution since the time step has to progressively decrease significantly anyway, in order to accommodate the abrupt spatial variation of the solution in the main direction of the flow. Therefore, spatial resolution in regions of excessive film growth controls computational cost. When the unsteadiness of the motion in the gas phase is accounted for, in order to capture the development of TS waves, the pressure and velocity fields in the two phases along with the film location are solved for simultaneously (defined in (2.2)–(2.11)). When a quasi-steady state is assumed for the gas phase, which is indeed the case when the liquid occupying the film is much more viscous than the gas ($\mu/\mu_w \to 0$), then the time stepping procedure is heavily dependent on the importance of film inertia. For relatively heavy films, $\mathfrak{M} < 1$ but not vanishing, the velocity field in the film along with the location of the interface have to be updated at the same time via time integration of (2.8) and (2.9). When film inertia is negligible, $\mathfrak{M} \to 0$, time stepping is performed on (2.12) only, involving the spatiotemporal evolution of the film thickness. In the last two cases a separate inversion takes place in the gas phase in order to obtain the velocity, pressure and displacement thickness fields for given location of the interface. The three cases described above involve progressively smaller numerical effort in terms of the size of the matrix that needs to be inverted at each time step. This process is formally described as

$$C_{ij}\dot{x}_j = F_i(\boldsymbol{x}) \overset{trapezoidal\ rule}{\longrightarrow} C_{ij}\frac{x_j^n - x_j^o}{\Delta t} - \frac{F_i(\boldsymbol{x}^n) + F_i(\boldsymbol{x}^o)}{2} = \boldsymbol{R}_i = 0, \tag{3.13}$$

where $\boldsymbol{x}$ is the unknown vector, C_{ij} is the mass matrix, superscripts n and o stand for the old and new time step, respectively, and $\boldsymbol{R}_i$ is the residual vector that incorporates nonlinear contributions. The residual vector becomes vanishingly small for the appropriate values of the unknown vector. The latter are obtained through the Newton–Raphson iterative process

$$\boldsymbol{A}_{ij}\left(x_j^{n,k} - x_j^{n,k+1}\right) = \boldsymbol{R}_i(\boldsymbol{x}^{n,k}), \quad \boldsymbol{A}_{ij} = \frac{C_{ij}}{\Delta t} - \frac{1}{2}\frac{\partial F_i}{\partial x_j^{n,k}}, \tag{3.14}$$

where $\boldsymbol{A}_{ij}$ denotes the Jacobian vector and k is the Newton's iterations count. When the flow in the gas phase is solved for separately, assuming a quasi-steady state, the mass matrix is absent and the Jacobian matrix only involves derivatives of right-hand side $F_i(\boldsymbol{x})$ with respect to the unknown vector $\boldsymbol{x}^k$.

In the context of this study, it was seen that the most time consuming step during the numerical simulation is the inversion of the Jacobian matrix $\boldsymbol{A}_{ij}$. In particular, it was estimated that the inversion of matrix $\boldsymbol{A}_{ij}$ consumes approximately 95 % of the total computational time needed to perform one time step. It should be stressed that direct inversion of matrix $\boldsymbol{A}_{ij}$ was not employed for the solution of matrix problem (3.14). Rather an iterative approach, in particular, generalized minimum residual (GMRES) method was opted for, as will be discussed in § 3.4. Therefore the term matrix inversion is used in the following in order to signify solution of a matrix

https://doi.org/10.1017/S0022112009990644 Published online by Cambridge University Press

problem of the type $\boldsymbol{A}_{ij}x_j = b_i$. In an effort to reduce computational cost as much as possible, we avoid constructing and inverting the Jacobian matrix in each time step. This action is based on the fact that we use considerably small time steps in which case the Jacobian is not expected to change significantly between subsequent time intervals. The only disadvantage of this approach is that Newton–Raphson loses its quadratic convergence and consequently the number of iterations may increase. Nevertheless, it was seen that the gain in computational time considerably exceeds the extra cost engendered by the additional iterations. The exact number of time steps over which the Jacobian can be taken as constant varies and it depends on the rate of evolution of the phenomena captured by the simulation. The specific number was obtained as part of a trial and error process. At the most, a maximum of 500 time steps was seen to be afforded by the algorithm without updating the Jacobian.

3.3. *Boundary conditions*

Besides the selection of the appropriate basis functions, imposition of proper boundary conditions plays an important role in the numerical solution. In the flow that we examine there is upstream influence that is introduced via the interaction law (2.4). If we use B-splines as basis functions we must introduce additional nodes and therefore additional equations to the problem. The fact that we do not know exactly what is happening at the right end of the simulation area may cause additional feedback that does not exist in reality. We can avoid this problem by using either free boundary conditions at the right end of the simulation area or periodic boundary conditions for all variables in the direction of flow. The free boundary condition is an equation that constrains the spline coefficients at one end without assigning a particular value for the variable. It is obtained if we equate the description for the first derivative of the variable based on its spline representation with the finite difference approximation of the derivative based on nodal values obtained via the spline representation. This is a common practice in the spline literature for obtaining constraints on the spline coefficients near a boundary (Prender 1989) in the absence of reliable end conditions. Alternatively, in order to avoid feedback influence we can use periodic boundary conditions for all variables in x direction. The extent of the simulation interval in the $\overline{Y}$ direction, $\overline{Y}_\infty$, is chosen so that the second partial derivative of velocity in the upper end of the simulation area approaches zero, $\frac{\partial^2 U}{\partial \overline{Y}^2}|_{\overline{Y}\to\infty} \to 0$. To this end the numerical solution is monitored at regular time intervals. When the displacement thickness increases significantly, due to film growth and onset of recirculation, the location of $\overline{Y}_\infty$ is moved further away from the plate in order to accommodate the above condition.

3.4. *Description of algorithms*

In this subsection we present an outline of the algorithms that have been employed in order to solve the problem numerically. As a starting point, at $t = 0$ a disturbance is imposed on the gas–liquid interface. When a quasi-steady state is considered in the gas phase, based on the disturbed interface, the flow in the gas phase is solved separately in order to furnish the shear stress and pressure distribution exerted on the liquid film as a result of the displaced flow in the gas phase, i.e. (2.2)–(2.5), without the temporal term in the x-momentum. Due to the nonlinearity of the problem the Newton–Raphson method is employed as described in § 3.2. With the updated values for shear stress and pressure distribution we solve the problem in the film and calculate the velocity field and shape of the interface, i.e. (2.6)–(2.11). When the film inertia is negligible, (2.12) is advanced in time in order to solely update the position of the interface. In both cases the trapezoidal rule is used for temporal integration

https://doi.org/10.1017/S0022112009990644 Published online by Cambridge University Press

and the interfacial position is then used as an input for the problem in the gas phase. Depending on the slope and curvature distribution of the new interfacial position the longitudinal distribution of mesh points is adapted. The sequential solution of the problems in the gas and liquid phase is continued for as long as necessary in order to capture the dynamic behaviour of the system.

A similar algorithm is applied when we solve the overall problem in order to study interfacial waves in the presence of TS. The only difference lies on the fact that the solution of the two phases is done simultaneously. Consequently, following the initial interfacial disturbance at $t=0$, the velocity and pressure fields along with the interfacial position are updated in a coupled fashion through time integration of (2.2), (2.8) and (2.9), subject to conditions (2.3)–(2.7) and (2.10)–(2.11). The time integration is advanced in this fashion for a time duration necessary to capture the advancement of TS waves and their interaction with the interfacial waves. As will be seen in § 4, due to the very fast evolution of the former waves, especially as the ratio μ/μ_w decreases, they reach the right end of the computational domain before any significant variation of the position of the interface is observed. Since interaction between the two types of waves is a central goal of the present study, time integration cannot proceed further unless the domain is extended considerably. However, as the two types of waves will have evolved quite apart with time their interaction will rapidly become very weak. Thus, as an alternate approach the transient evolution of the gas phase, and consequently of TS waves, is turned on after an amount of time necessary for significant growth of interfacial waves to have taken place. More details are provided in § 4 dedicated on the discussion of numerical results for gas-film interaction.

Besides lagging the updating of the Jacobian, in order to further reduce computational cost the linearized system (3.14) that has to be solved at each Newton iteration is treated iteratively with the GMRES method rather than by direct inversion (Saad & Schultz 1986). Preconditioning is done using incomplete lower–upper factorization (ILU). ILU is based on Gauss elimination in a fashion that eliminates a certain number of elements in specific positions outside the main diagonal.

The final step in our effort to reduce computational cost is based on the fact that the disturbances under consideration do not cover the entire domain in the longitudinal direction. Thus, in order for the simulation to provide the desired accuracy, grid refinement need only be confined in regions where the disturbances appear at a certain time instant. As a result, the load in computational time as well as storage is significantly reduced. Moreover, due to the convective character of the disturbances the grid must be adapted in order to follow the evolution of the waves. The method that is employed in order to construct the adapted mesh is based on the redistribution of grid nodes via an appropriate weight function $w(X)$. In this fashion, the grid becomes dense only in the areas where the weight function is large. The following equation is thus obtained that can be used to calculate the new grid:

$$\int_0^{X_i} w(\chi)\,\mathrm{d}\chi = \frac{i-1}{\mathrm{N}-1}\int_0^{L} w(\chi)\,\mathrm{d}\chi, \quad i=2,3,\ldots N-1, \quad w(X)=(1+d|h_X|+b|h_{XX}|), \tag{3.15}$$

where $h_X=\partial h/\partial X$, $h_{XX}=\partial^2 h/\partial X^2$ and h denotes the shape of the interface. Coefficients b and d correspond to the influence that interfacial slope and curvature bear on the desired grid density. Their values vary between 0 and 1. Additional

https://doi.org/10.1017/S0022112009990644 Published online by Cambridge University Press

Wave length	2.3
Period	0.8
Group velocity	4.5

TABLE 1. Results of linear theory for the most unstable wave of TS waves at $x = 1$.

information regarding one-dimensional grid adaptation as well as criteria for choosing the appropriate weight function can be found in Thompson, Warsi & Mastin (1995).

3.5. *Numerical validation for interaction with a solid obstacle*

In order to compare the effectiveness of quadratic Lagrangian and cubic B-splines as basis functions we simulate the flow of air above a flat plate in the case of an instantaneous linear disturbance on the longitudinal velocity of the type shown in (2.14*a*), $d = 0.001$ and $W = 4$, that is imposed at longitudinal and transverse positions $x = 1$ and $\bar{Y} = 2$; $\bar{Y}_\infty = 8$. Our aim is to capture the characteristics of TS waves as close as possible to the theoretical predictions based on the linear dispersion relation (Lin 1946; Smith 1979*a*) and to the findings of numerical simulations in the nonlinear regime (Duck 1985; Smith & Burggraf 1985):

$$\frac{\mathrm{d}Ai}{\mathrm{d}z} + \frac{\left(kH_0^2C\right)^{1/3}}{A^2} i^{1/3} k H_0 \int_\infty^z Ai(t)\,\mathrm{d}t = 0, \quad z = -\frac{H_0\omega i^{1/3}}{\left(kH_0^2C\right)^{2/3}}, \quad C(x) = \frac{x^{1/4}\sqrt{0.664}}{H_0(x)} \tag{3.16}$$

with k and ω denoting the wavenumber and frequency of the wave, respectively, and $H_0(x)$ the base flow film thickness provided in (2.1). The problem formulation is the same as the gas phase formulation outlined in (2.2)–(2.5), with the position of the interface set to zero and the no-slip no-penetration boundary conditions imposed on the flat plate. In order to eliminate the dependence on variable x from the Blasius solution we introduce the following transformed variables (Jenson *et al.* 1975; Ruban 1978; Terent'ev 1981, 1984; Smith & Burggraf 1985; Ryzhov & Terent'ev 1986):

$$\frac{T}{b^{-3/2}} \to T, \quad \frac{X}{b^{-5/4}} \to X, \quad \frac{\bar{Y}}{b^{-3/4}} \to \bar{Y}, \quad \frac{U}{b^{1/4}} \to U, \quad \frac{\Psi}{b^{-1/2}} \to \Psi,$$
$$\frac{P}{b^{1/2}} \to P, \quad \frac{A}{b^{-3/4}} \to A, \tag{3.17}$$

where $b = \partial U_0/\partial y\,(x, y = 0) = 0.332/\sqrt{x}$, is the Blasius shear stress evaluated on the plate with $y = y'/LRe^{-1/2}$. Estimates of the wavelength $2\pi/k$, period $2\pi/\omega$ and group velocity $\mathrm{d}\omega/\mathrm{d}k$ of the most unstable wave are given in table 1, as derived from linear stability analysis.

First, we solve the problem by using quadratic Lagrangian basis functions. What we observe is that this procedure fails to give reliable results. More specifically, the resulting wavelength depends on the spatial interval dX and is always approximately equal to $4dX$. In figure 2 the displacement thickness is shown for dimensionless longitudinal step size $\Delta X = 0.5$ and 0.25 and a time step $\Delta t = 0.001$, whereas in table 2 the numerically calculated wavelengths of the disturbance are given for three different mesh sizes. The frequency and wavelength of the disturbance are extracted from the numerical solution via FT the displacement thickness A, profile evaluated either at a certain time instant T_0, or at a certain longitudinal position X_0, that are

https://doi.org/10.1017/S0022112009990644 Published online by Cambridge University Press

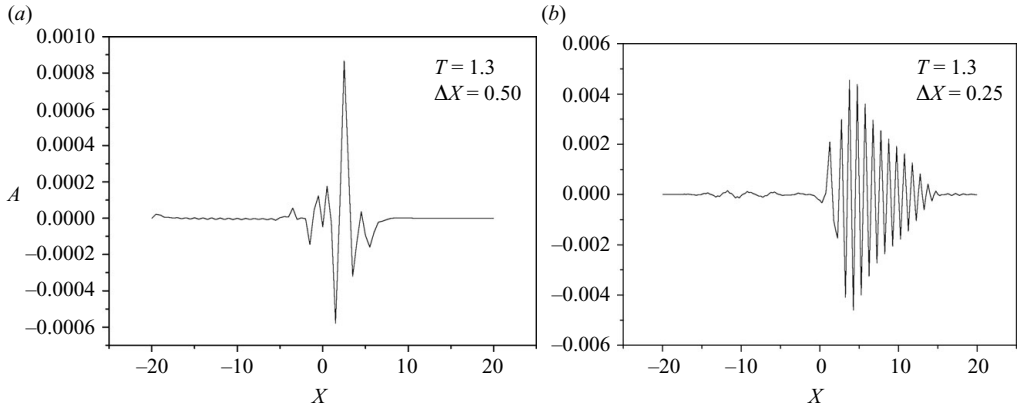


FIGURE 2. Displacement thickness for the TS waves with mesh size: (*a*) $\Delta X = 0.5$ and (*b*) $\Delta X = 0.25$, using Lagrangian basis functions; $\Delta T = 0.001$.

Spatial interval ΔX	0.5	0.33	0.25
Wavelength	1.78	1.33	1

TABLE 2. Computed wavelength of the most unstable wave for TS waves by using quadratic Lagrangian basis functions.

Spatial step ΔX	0.5	0.33	0.25
Wavelength	2.2	2.2	2.2
Period	0.83	0.83	0.83
Group velocity	4.6	4.6	4.6

TABLE 3. Computed attributes of the most unstable wave for TS waves by using B-cubic splines as basis functions.

quite large so that asymptotic linear growth is established. For example,

$$A(X_0, T) = \sum_{n=-N/2}^{n=N/2} c_n(X_0) \mathrm{e}^{\mathrm{i}\frac{2n\pi}{T_L}T}, \quad c_n = \frac{1}{T_L}\int_0^{T_L} A\,(X_0, T)\,\mathrm{e}^{-\mathrm{i}\frac{2n\pi}{T_L}T}\,\mathrm{d}T, \quad N\Delta T = T_L, \tag{3.18}$$

where T_L is the time interval over which the transform is taken and X_0 is the longitudinal position that is sampled. The wavelengths are obtained in a similar fashion. The maxima of the Fourier spectra, $\max_{1\leqslant n\leqslant N/2}|c_n|$, are registered and are associated with the appropriate time or length scales, $\omega_n = 2n\pi/T_L$, $k_n = 2n\pi/L$. The x-coordinate in the FT spectra to be presented in the following denotes the frequency, $\nu = 1/T_P$ or $\nu = 1/\ell$, corresponding to the period or wavelength associated with a certain peak. The group velocity u_G is calculated simply by locating the absolute maxima of the travelling wave packet, X_{1m}, X_{2m}, corresponding to the wave with the largest growth rate at two different time instants, T_1, T_2, such that $X_{im} \gg 2\pi/k_n$ and $T_{im} \gg 2\pi/\omega_n$ for $i = 1, 2$, and performing numerical differentiation; $u_G = (X_{2m} - X_{1m})/(T_{2m} - T_{1m})$. Even though this is a rather simplistic way of obtaining the group velocity it provides quite reliable estimates as will be seen in the following.

Then we repeat the calculation by using B-cubic splines as basis functions. In this case we find that the results are accurate to almost the third significant digit and do not depend on the spatial step. Table 3 illustrates this fact for the same mesh sizes that

https://doi.org/10.1017/S0022112009990644 Published online by Cambridge University Press

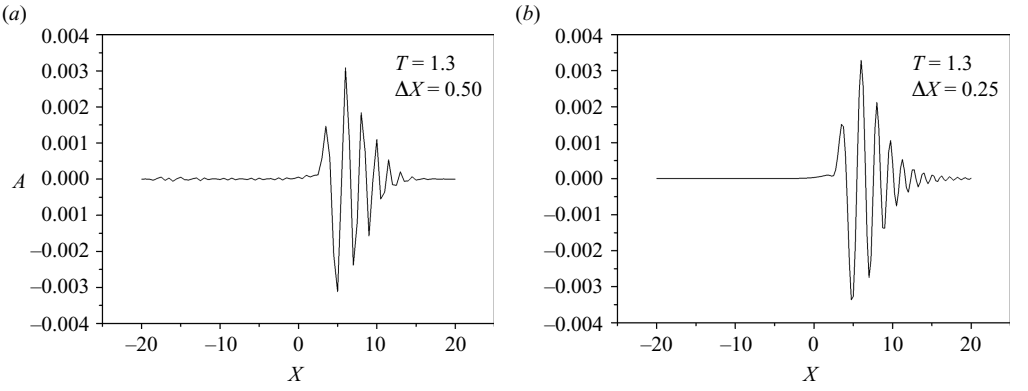


FIGURE 3. Displacement thickness for the TS waves with mesh size: (*a*) $\Delta X = 0.5$ and (*b*) $\Delta X = 0.25$, using cubic B-splines as basis functions; $\Delta T = 0.001$.

were used in the simulations with quadratic Lagrangian basis functions. Clearly, the results for the wavelength, period and group velocity are grid independent and agree with the results of linear theory given in table 1. Figure 3 reproduces the displacement thickness for the cases shown in figure 2, indicating pointwise convergence with mesh refinement. The convectively unstable nature of the TS waves is also recovered, as indicated by the travelling wave packet characterizing the spatiotemporal evolution of the displacement thickness. The wave-packet characteristics, i.e. group velocity, period and wavelength of the most unstable waves, are also in very good agreement with previous calculations in the linear regime performed by Ryzhov & Terent'ev (1986), via a Fourier–Laplace transform in space and time. The superior behaviour of cubic splines is due to the fact that they are of higher order than quadratic Lagrangian basis functions. Moreover, they have continuous first and second derivatives, they are characterized by non-local support, i.e. each global B-spline extends over four rather than two consecutive elements, and that amounts to an inherent smoothing effect on the interpolated unknown functions. The inefficiency of quadratic Lagrangian basis functions to keep up with the B-splines in problems involving large interfacial distortions has been observed in other contexts as well, e.g. in the study of the dynamics of bubbles and drops in both axisymmetric and three-dimensional flow domains (Pelekasis *et al.* 1992; Lac *et al.* 2004).

Having chosen the appropriate basis functions we proceed to test the numerical code in a case of airflow above a small unsteady hump. We consider the hump that Duck (1985) used in his study of laminar flow over unsteady obstacles, where he was able to capture the nonlinear evolution of TS waves. Using the triple deck scales, the exact shape of the hump reads as

$$F(x,t) = \begin{cases} h\dfrac{\sin(t/\beta^2)}{1+x^2}, & 0 < t < \pi\beta^2/2 \\ h\dfrac{1}{1+x^2}, & t > \pi\beta^2/2 \end{cases}, \quad \beta = \frac{U_o^{1/2}}{\omega^{1/2}L^{1/2}Re^{-1/8}}, \tag{3.19}$$

where h is a measure of the size of the obstacle and β is associated to the dimensionless oscillation frequency of the hump; $\beta \approx 0.66$ corresponds to neutral disturbances in the lower TS branch whereas disturbances with $\beta < 0.66$ excite unstable modes. The governing equations are (2.2)–(2.5) with μ/μ_w set to one and the standard

https://doi.org/10.1017/S0022112009990644 Published online by Cambridge University Press

no-slip no-penetration conditions imposed on the hump. The motion of the obstacle is prescribed so that it contains an initial start-up process followed by a steady shape.

Figure 4 shows the spatiotemporal evolution of the displacement thickness in the case of a hump with $h = 0.1$ and $\beta = 1$. The presence of the hump disturbs the flow and, even though $\beta = 1$ lies within the range of stable disturbances, the disturbed spectrum initially contains all the wavelengths out of which the fastest growing TS wave eventually dominates through linear growth. The small indentation in the displacement thickness profile behind the travelling wave packet is a signature of the shape of the obstacle after the oscillatory start-up process is over. Overall, for fixed X, as time increases oscillations die out leading to a steady state. The wavelength dominating the wave packet is found to be 2.45, while the numerical group velocity is equal to 4.3. These results are in agreement with the predictions of linear theory in table 1 and previous linear calculations (Ryzhov & Terent'ev 1986). As the dominant wave packet further evolves in time it does not exhibit any sideband instabilities. However, more unstable modes become evident forming secondary wave packets of smaller amplitude, clearly shown in figure 4(f), corresponding to greater wavenumbers and higher frequencies. The FT of the displacement thickness at appropriately selected time and spatial locations verify the relevant length and time scales (figures 4g and 4h). The mechanism underlying growth of such modes is not clear. It should be stressed that during the late stages of the phenomenon the amplitude of the leading wave packet is large enough for nonlinear growth to take place. According to the dispersion relation of the TS waves, large wavenumbers belong to the unstable regime and consequently they gradually grow with time. Weakly nonlinear analysis and simulations of the development of high frequency TS waves performed by Smith (1986) indicate growth and spreading of the dominant wave packet during the initial stages and broadening of the wavelength spectrum and spiked behaviour during the late stages of their development due to vorticity bursts from the viscous sublayer. The latter process is significantly enhanced by nonlinearity. As an additional reason, the short-wavelength wave packets shown in figure 4 may arise due to the non-local nature of the moving obstacle instigating the motion. Such wave packets were not obtained in the present study when the initial disturbance was of the form of a delta function in space. Such a behaviour is observed in numerical solutions of Schrodinger's equation that is known to give rise to travelling wave packets upon imposition of a disturbance that is not sufficiently localized. It should be pointed out, however, that local convergence was not obtained upon mesh refinement of the simulations presented in figure 4. This may be due to the very small wavelength of the emerging structures that reduces the accuracy of the simulations. Numerical simulations performed by Cassel *et al.* (1995, 1996) on supersonic flow over a compression ramp via the interactive boundary layer formulation, produced a stationary wave packet as a result of an absolute instability of the boundary layer that is associated with an inflection point in the streamwise velocity profile. This occurred beyond a threshold value of the ramp angle and inside the recirculation region of the ramp. Upstream of the stationary wave packet the simulations produced additional oscillations in cases of strong wall cooling, for which the wall shear develops a very steep slope ahead of the separation region. More accurate simulations recently performed by Fletcher *et al.* (2004) showed that such oscillatory behaviour is entirely a numerical artefact arising due to the steep change in the wall shear. We believe that this is probably not the case here since such steep changes only appear in the flow field during the very late stages of the evolution of the dominant wave packet and manifest themselves in the form of spikes in the displacement thickness in figures 4 and 5. The latter is an effect that

https://doi.org/10.1017/S0022112009990644 Published online by Cambridge University Press

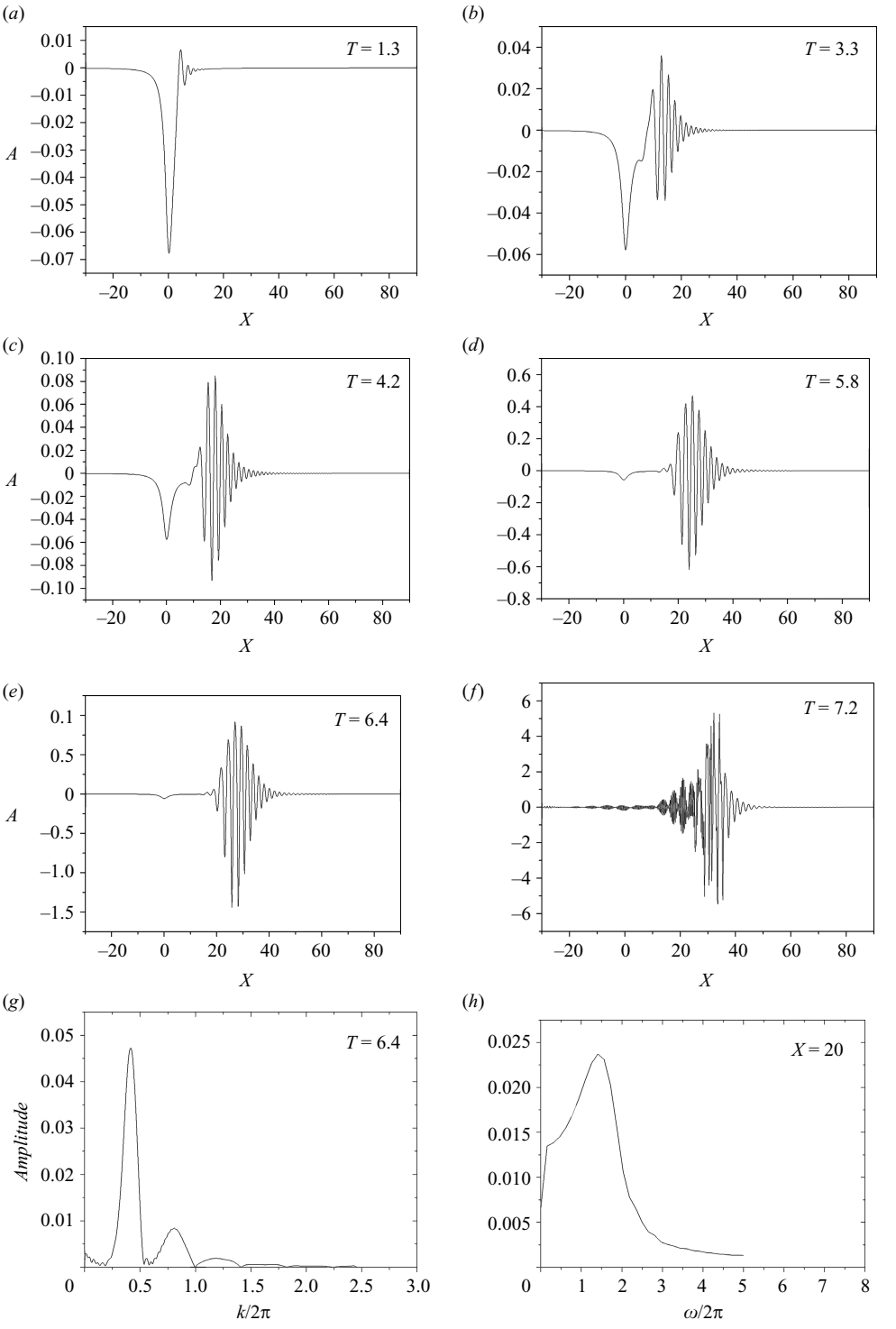


FIGURE 4. (*a*)–(*f*) Spatiotemporal evolution of the displacement thickness in the case of an unsteady hump with $h = 0.1$ and $\beta = 1$, (*g*) spatial FT of the displacement thickness at $T = 6.4$, (*h*) time FT of the displacement thickness at $X = 20$.

https://doi.org/10.1017/S0022112009990644 Published online by Cambridge University Press

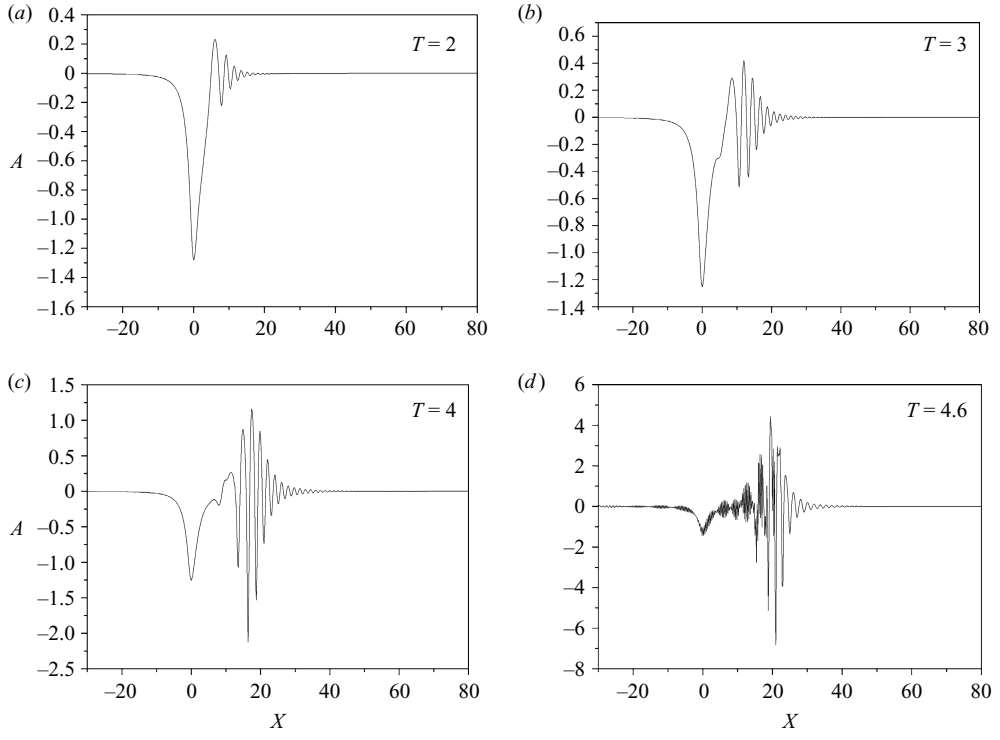


FIGURE 5. Spatiotemporal evolution of the displacement thickness in the case of an unsteady hump with $h = 2$ and $\beta = 1$.

is theoretically predicted to eventually appear in the evolution of TS wave packets (Smith 1986, 1988) whereas the onset of oscillatory behaviour in the simulations takes place at an earlier stage. Additional mesh refinement was not pursued in the present study since its focus lies in a different form of interaction.

A similar behaviour is observed as the amplitude of the hump pulsation grows. We have used humps with obstacle size h ranging between 0.1 and 2 and we have confirmed the fact that the disturbance amplitude primarily affects the time needed for the secondary modes to develop. The greater the amplitude is, the sooner the most dangerous wave grows. Figure 5 illustrates this pattern for flow above an unsteady hump with maximum amplitude 2, also indicating a steady state solution for flow over the steady form of the obstacle as time increases. Eventually the simulations have to stop due to growth of progressively smaller waves that are too difficult to capture by the available discretization. During the late stages of the phenomenon the leading wave packet tends to exhibit spiked behaviour and singularities in the displacement thickness and pressure distribution in the manner discussed in the previous paragraph.

4. Results and discussion for interaction with a liquid film

4.1. *Growth of Tollmien–Schlichting and interfacial waves*

In this section we first address the full problem of a boundary layer interacting with a thin film, in the sense that not only are inertia effects accounted for in the film but also we allow for transient effects to take place in both phases. This allows for coinstantaneous growth of TS and interfacial waves. The study focuses on the cases

https://doi.org/10.1017/S0022112009990644 Published online by Cambridge University Press

of a water film or a film of de/anti-icing fluid being dragged by a boundary layer of air, which sets the viscosity ratio μ/μ_w to relatively low values. Properties for the latter system are obtained from Ozgen *et al.* (1998) and Hendrickson & Hill (1987), $\mu/\mu_w = 1.67 \cdot 10^{-6}$ and $\rho/\rho_w = 0.001$, while a flow arrangement characterized by a test section of length $L \approx 30$ cm and a free stream velocity U_∞, ranging between 10 and 40 m s^{-1} is envisioned as it covers a wide range of available experimental investigations. In this context, when $L \approx 30$ cm and $U_\infty \approx 30$ m s^{-1} $\overline{Fr} = 92\,699$, $3.94 \cdot 10^4$ and $\overline{We} = 46\,59.88$ for the cases of water and deicing fluid respectively. The film thickness necessary for the triple-deck approach to be valid is $H_f \sim LRe^{-5/8} \approx 0.06$ mm which is on the order of film measurements on airfoils under simulated rainfall conditions. The mesh characteristics in the bulk of the simulations are $\Delta x = 0.2$, $\Delta y = 0.4$, $\Delta t = 0.001$, $Y_\infty = 10$. Simulations with $\Delta x = 0.1$ and $\Delta y = 0.2$ were conducted as well in order to capture effects related with film inertia that leads to smaller wavelengths and more intense recirculation patterns, but also to validate the results via mesh refinement. Two different types of disturbances are employed, namely impulsive and time periodic. The location of the disturbance in the context of the base flow is determined through parameter x_0 and normally refers to (2.1*a*) pertaining to the case of rainfall. The results exhibit negligible variation if the case of constant flow rate is selected (defined in (2.1*b*)), since it is primarily the shear rate $\lambda = \partial U_0/\partial Y'\,(x_0, Y' = 0) = 0.332/\sqrt{x_0}$ and film thickness H_0 that affect the flow stability and they are comparable in either case. The former parameter does not vary between the two base solutions, provided x_0 is the same. The film thickness H_0, on the other hand, may be different. The choice between the two base flow arrangements, (2.1*a*) versus (2.1*b*), can play a role in the investigation of global instabilities but, as will be seen in the next subsection, such phenomena are subdominant to the growth of the most unstable wave in the nonlinear regime. Unless otherwise specified these are the attributes of the numerical simulations to be presented in the following.

As a preliminary test we consider the case of a water film upon the interface of which an initial disturbance is imposed at $x_0 = 1$, characterized by amplitude $d = 0.001$ and initial film thickness $H_0 = 2.45$. Owing to the small amplitude of the disturbance linear theory describes the onset of the motion. Figure 6(*a*) portrays the shape of the interface at time $t = 0.6$, and it can be clearly seen that before the interfacial wave exhibits any significant growth the TS waves have already been formed and reached the right end of the simulation grid. Their signature on the location of the interface is not significant but is still detectable. The evolution of the TS waves can be better observed in graph of figure 6(*b*) showing the displacement thickness in the gas phase. By performing FT analysis on this signal we can calculate the wavelength of TS waves which is equal to 9.3. Similarly the period of the TS waves is recovered, $T_{TS} = 0.07$, by registering the time series of the displacement thickness at a certain X position (figure 6*c*). The graphs verify the convectively unstable nature of the TS waves. It should be stressed that upon application of transformation (3.17) with $x = 1$ the values provided in table 1 are recovered. The group velocity, $u_G = 195$, is obtained in the manner explained in the previous section via the absolute maxima of the travelling wave packet. All the aforementioned quantities are in agreement with the predictions of linear analysis for TS waves as they evolve either on their own, (4.1), or coupled with a liquid film (Timoshin 1997; Pelekasis & Tsamopoulos 2001). Both types of stability analysis furnish similar results due to the small viscosity ratio, $\mu/\mu_w = 0.018$, indicating convective instability as the mode for growth of the unstable waves. Moreover, the growth of the interfacial waves is unaffected by the much faster growth of the TS waves, as will also be illustrated in the following.

https://doi.org/10.1017/S0022112009990644 Published online by Cambridge University Press

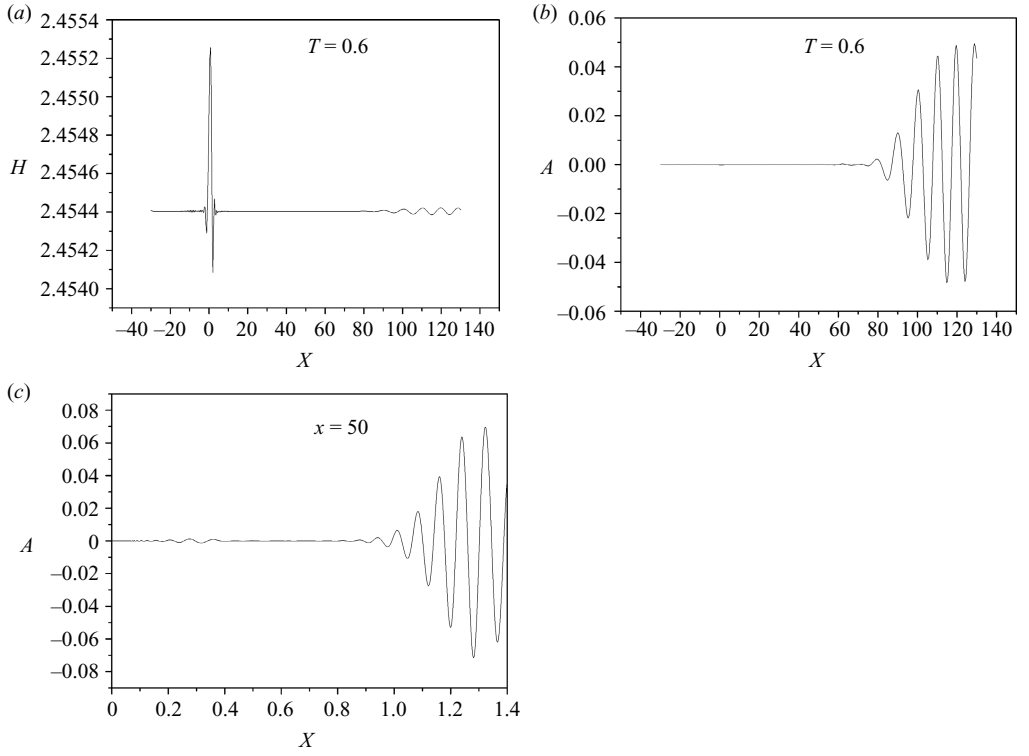


FIGURE 6. Simulation of the overall problem in response to an initial disturbance on the interface at $x = 1$ with $d = 0.001$: (a) shape of the interface at $t = 0.6$, (b) displacement thickness profile at $t = 0.6$ and (c) time series of the displacement thickness at $X = 50$.

As a second test we set the same disturbance on the interface while maintaining the quasi-steady state in the gas phase. Thus, we allow the interfacial waves to develop up to a certain point in time, i.e. $T = 6$. Then at that particular time we impose a small disturbance, $d = 0.001$, on the axial velocity in the bulk of the boundary layer ($X = 0$, $Y = 2$). At the same time we activate transient effects inside the boundary layer. In this fashion, we can monitor the development of TS waves after interfacial waves have been formed and therefore explore the possibility of interaction between them. Figures 7(a) and 7(b) depict the shape of the interface before we impose the disturbance in the gas phase at $T = 6$, and the time series of the interfacial position at $X = 10$, respectively. Performing FT on these graphs we obtain the relevant space and time scales of the growing wave; the period $T_{in} = 2.8$ is while the wavelength $l_{in} = 3.2$. They both conform to the findings of linear analysis for growth of interfacial waves due to shear from a surrounding boundary layer (Timoshin 1997; Pelekasis & Tsamopoulos 2001). The group velocity is also estimated, $u_G = 1.4$, in agreement with linear theory, thus concluding that the wave packet illustrated in figure 7(a) corresponds to the fastest growing interfacial wave. It should be stressed, however, that according to linear theory interfacial waves of the air/water system are absolutely unstable in this parameter range. According to linear theory, the fastest growing wave is expected to appear in an absolutely unstable wave packet, which will contain waves with zero group velocity. In the present case the linear growth of this particular wave is marginal as compared to the most unstable one, hence the former occupies the

https://doi.org/10.1017/S0022112009990644 Published online by Cambridge University Press

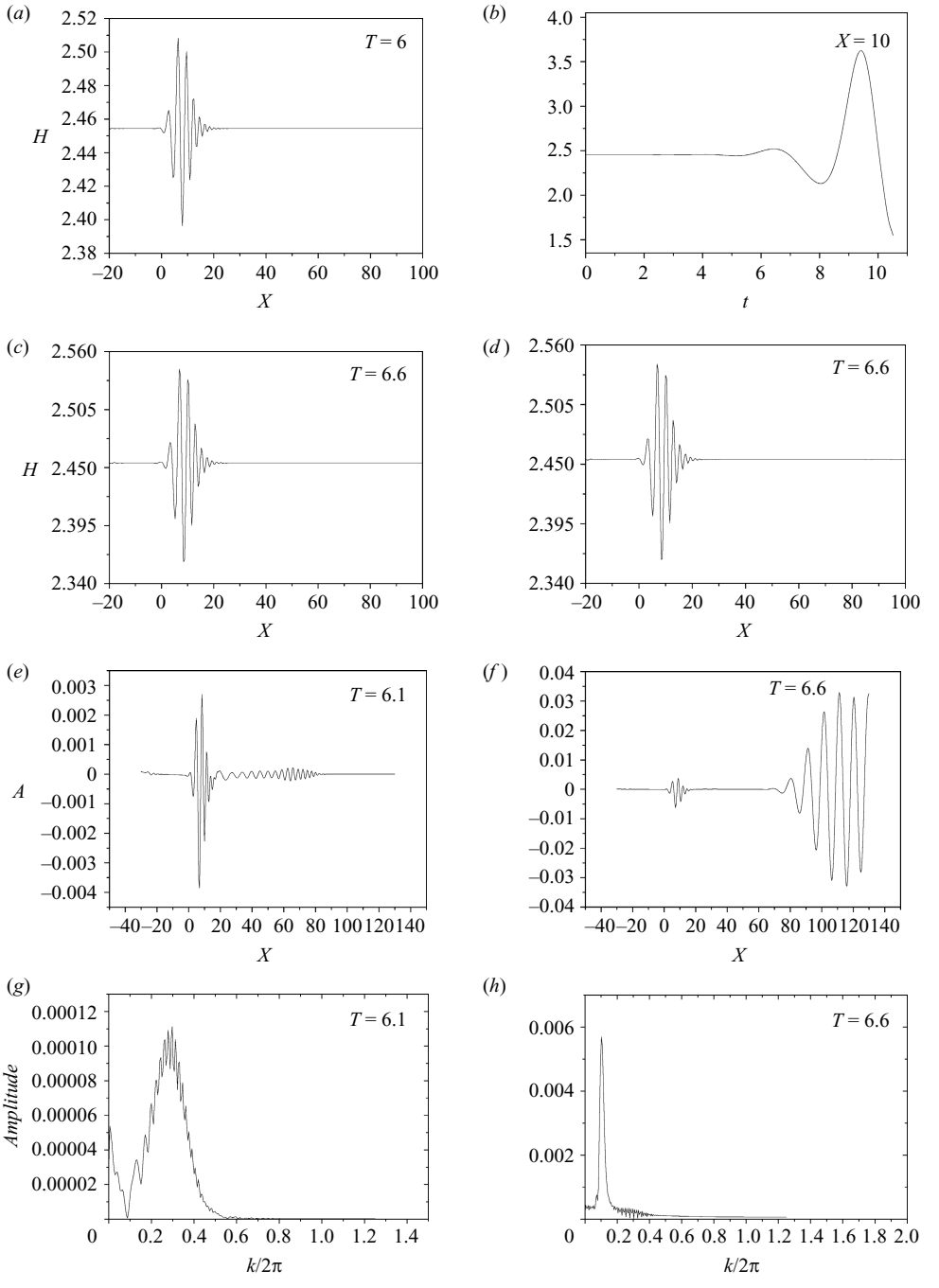


FIGURE 7. Simulation of the overall problem when a second disturbance is imposed in the bulk of the boundary layer at $T = 6$: (*a*) shape of the interface before we impose the second disturbance, (*b*) time series of the interfacial position at $X = 10$, (*c*) shape of the interface at $T = 6.6$ without imposing the second disturbance, (*d*) shape of the interface at $T = 6.6$ with the imposition of the second disturbance and relaxing the quasi-steady state assumption, (*e*) displacement thickness of the gas phase at $T = 6.1$, (*f*) displacement thickness of the gas phase at $T = 6.6$, (*g*) FT of the displacement thickness at $T = 6.1$ and (*h*) FT of the displacement thickness at $T = 6.6$.

https://doi.org/10.1017/S0022112009990644 Published online by Cambridge University Press

left-most part of the interfacial wave packet. This is manifested in figure 7 by the fact that the interfacial wave packet never quite leaves the origin of the x-axis which is also the location of the imposed initial disturbance. This issue will be elaborated in the next subsection where it will be seen that this pattern is generally true for the air/water system.

Figures 7(c) and 7(d) show the shape of the interface at $T = 6.6$ without and with the imposition of the disturbance in the bulk of the boundary layer. Clearly the appearance and growth of TS waves does not affect the evolution of the interfacial waves, as the two shapes are identical and conform to the evolution of the most unstable wave packet according to linear theory. In fact, not much has happened on the interface in the time interval between $T = 6$ and 6.6. On the contrary the TS waves have evolved quite significantly in this time frame as can be gleaned from figures 7(e) and 7(f) depicting snapshots of the displacement thickness at these two time instants. In figure 7(e), shortly after the transient effects are turned on in the gas phase, an interesting superposition of different wave packets is depicted in the profile of the displacement thickness. More specifically, the signature of the wave packet pertaining to the interfacial wave is illustrated on the left. It is dominant at this time instant, since the TS waves have not yet had enough time to evolve, yet it appears as a fixed obstacle since its group velocity is much smaller than that of the TS waves. Ahead of the interfacial wave two more wave packets are exhibited in figure 7(e) corresponding to the TS waves generated in the gas phase in response to the oscillating interface and to the fastest growing TS wave. The former TS waves move at a larger group velocity hence they are ahead of the fastest growing wave, but they grow at a slower rate. The wavelength of this wave packet is the same as the wavelength of the interfacial wave only it moves much faster. It is smaller than the wavelength of the fastest growing TS wave and, as predicted by the dispersion relation of the TS waves, it is also unstable. It should be stressed that the period of oscillation of the interfacial wave, $T_{in} = 2.8$, is much larger than the one of the most unstable TS wave, $T_P = 0.07$. Thus, the leading wave in figure 7(e) is equivalent to the wave packet that is formed when a boundary layer interacts with a stationary grooved boundary characterized by the wavelength of the interfacial wave. It is a result of the deviation of the shape of the interface from the classical pulse-like shape, as the non-local nature of the former leads to the formation of additional wave packets. Similar wave formation has been observed in earlier studies on the effect of oscillating obstacles on the development of TS waves (Duck 1985). Performing an FT on the profile shown in figures 7(e) and 7(f) recovers the relevant length scales, figures 7(g) and (7h), verifying the above picture. At time $T = 6.6$ the most unstable wave has fully evolved and surpassed in amplitude the interfacial wave while it has reached the right end of the computational domain. The wave packet corresponding to TS waves growing in response to the deformation of the interfacial wave has already exited the domain due to its larger group velocity, without ever reaching the level of amplitude exhibited by the fastest growing wave.

Nevertheless, the appearance of this wave packet may explain observations of transition to turbulence in the presence of viscous films that is dominated by smaller wavelengths than the ones corresponding to the most unstable TS wave. In fact, as pointed out elsewhere (Timoshin 1997) setting the density ratio to one while maintaining a low viscosity ratio reduces the wavelength corresponding to maximum growth rate of TS waves thus bringing about the possibility of identical dominant wavelengths for the two types of instabilities, for the appropriate value of surface

https://doi.org/10.1017/S0022112009990644 Published online by Cambridge University Press

tension. Figure 7(*e*) indicates this tendency for the two leading TS waves to merge and form one wave that will grow much faster than the classical TS wave. The onset of TS waves is expected to become quite abrupt when ρ/ρ_w approaches unity, in which case the wavelengths for maximum growth of the interfacial and TS waves become almost identical. It should also be pointed out that, perhaps, such a coincidence in wavelengths is not imperative for bypassing the classical root to turbulence since even when they are not so close in magnitude, as is the case for the air–water system, there is an identifiable TS wave dominated by the wavelength of the interfacial waves. Depending on the dynamics of that particular wave and its susceptibility to three-dimensional disturbances transition to turbulence may occur much faster than expected.

Finally, it should be stressed that increasing the amplitude of the initial disturbance does not alter the above picture, apart from reducing the time scale over which the relevant phenomena evolve. Examining the case with de/anti-icing fluids interacting with air only accentuates the above effects owing to their much larger viscosity.

4.2. *Evolution of interfacial waves in the limit of small viscosity ratio,* $\mu/\mu_w \ll 1$

Due to the very disparate time scales governing the development of the interfacial and TS waves, when the film consists of water or de/anti-icing fluid, we focus on the limiting case of negligibly small viscosity ratio, $\mu/\mu_w \to 0$, and consequently assume a quasi-steady state in the gas phase. Based on the discussion in the first part of § 4 this is a well-justified assumption, for systems characterized by small viscosity ratio, which essentially allows us to decouple the development of interfacial waves from that of the TS waves.

4.2.1. *Response in the linear regime*

As a first step we want to cross-check the validity of our numerical methodology against linear theory as time advances, in response to small-amplitude disturbances. As a starting point we consider the special case for which parameter $\mathfrak{M} \to 0$ and consequently inertia forces in the liquid film are negligible. This is the case when the liquid is much more viscous than the gas, to the extent that the viscosity ratio dominates the typically large density ratio ρ_w/ρ, which is especially true for most de/anti-icing fluids. To this end we consider the flow of air above a deicing fluid that has been observed experimentally (Hendrickson & Hill 1987) and studied via linear stability analysis (Yih 1990; Ozgen *et al.* 1998) in order to obtain the relevant space and time scales. The parameters of the above experiment are used only as an example of a real case of a deicing fluid and there is no intention to further examine the experimental results since it was shown by Ozgen *et al.* (1998) that the waves observed in the experiments are TS waves. We choose an initial dimensionless height $H_0 = 2.076$ and shear rate $\lambda = 0.371$, corresponding to a film thickness at the base state $H_f \approx 0.15$ mm and an initial disturbance imposed at $x_0 = 0.8$ on the plate. Much larger film thicknesses were measured by Hendrickson & Hill 1987, e.g. on the order of 1 mm, yet we decided to use a lower value in order to justify dropping inertia effects. We introduce an impulsive linear disturbance ($d = 0.001$) and calculate the characteristics of the resulting wave. According to linear theory for the above set of parameters the dominant interfacial instability is convective. This is determined by examining the linear dispersion relation for interfacial waves in the limit of negligible

https://doi.org/10.1017/S0022112009990644 Published online by Cambridge University Press

	Linear theory with and without inertia	Numerical results with and without film inertia
Wavelength	3.47	3.53
Period	2.32	2.34
Group velocity	2.2	2.26

TABLE 4. Most unstable wave characteristics for interfacial waves of the air deicing system predicted analytically and computed numerically with the two different models, with and without inertia effects; $x_0 = 0.8$, $H_0 = 2.076$.

inertia effects, $\mathfrak{M} \to 0$ (Timoshin 1997; Pelekasis & Tsamopoulos 2001):

$$\omega = kH_0 \frac{\partial U_0}{\partial Y'}\bigg|_{Y'=0} - \frac{iH_0^3k^4}{3\overline{We}} - i\frac{(\rho_w/\rho - 1)}{\overline{Fr}}k^2\frac{H_0^3}{3} + \frac{H_0^2}{2}\left(-\frac{\partial U_0}{\partial Y'}\bigg|_{Y'=0}\right) \times \frac{Ai(z=0)\left(ik\,\dfrac{\partial U_0}{\partial Y'}\bigg|_{Y'=0}\right)^{2/3} k\,|k| - \dfrac{2}{3}\left(ik\,\dfrac{\partial U_0}{\partial Y'}\bigg|_{Y'=0}\right) H_0 k\,|k|\,Ai'(z=0)}{|k|\left(ik\,\dfrac{\partial U_0}{\partial Y'}\bigg|_{Y'=0}\right)^{1/3}\int_\infty^0 Ai\;\mathrm{d}z + Ai'(z=0)\left(\dfrac{\partial U_0}{\partial Y'}\bigg|_{Y'=0}\right)^2}. \quad (4.1)$$

The motion of the dominant wave packet is clearly illustrated in figure 8 depicting snap-shots of the interface. Table 4 provides the characteristics of the dominant wave as obtained via FT of the numerically calculated interfacial position and predicted by linear stability analysis, indicating very good agreement. One can also note the progressive spreading of the advancing wave packet predicted by linear theory. In fact, the speed by which the left and right fronts of the wave packet move is indicated in figure 8, by means of the corresponding rays emanating from the origin and following the left and right edges of the wave packet, and correlates well with the prediction of linear theory.

Regarding the quality of the numerical solution figure 8(f) illustrates an interesting phenomenon. As time evolves an additional wave packet appears at the left end of the computational domain and is convected downstream. Performing FT in a region around it we confirm that it also possesses the attributes of the most dangerous wave in terms of wavelength period and group velocity provided in table 4. It is a result of the truncation of the flow domain, which is really infinite, and corresponds to the response of the flow field to an impulsive disturbance of infinitesimally small amplitude at the left end of the computational domain. As we follow it downstream it exhibits all the characteristics of linear growth of the unstable wave packet that were discussed above. This is a recurring theme in our simulations and as will be illustrated in figure 12(f) the wave packet emanating from the left edge of the computational domain can even reach the preliminary stage of saturation. This process however will not be fully carried out since, as will be discussed in the following, it is disrupted by spike formation. As long as this wave packet remains far from the one that emerges in response to the main disturbance at $X = 0$ it cannot affect the overall numerical solution since, as prescribed by the interaction law in (2.4), the strength of interaction between different portions of the flow field drops like the inverse of their distance. Indeed, mesh refinement has verified this fact providing the same evolution of the leading wave packet irrespective of the dynamics of the one that emanates from the left corner of the domain. Pertaining to mesh refinement tests it should be pointed

https://doi.org/10.1017/S0022112009990644 Published online by Cambridge University Press

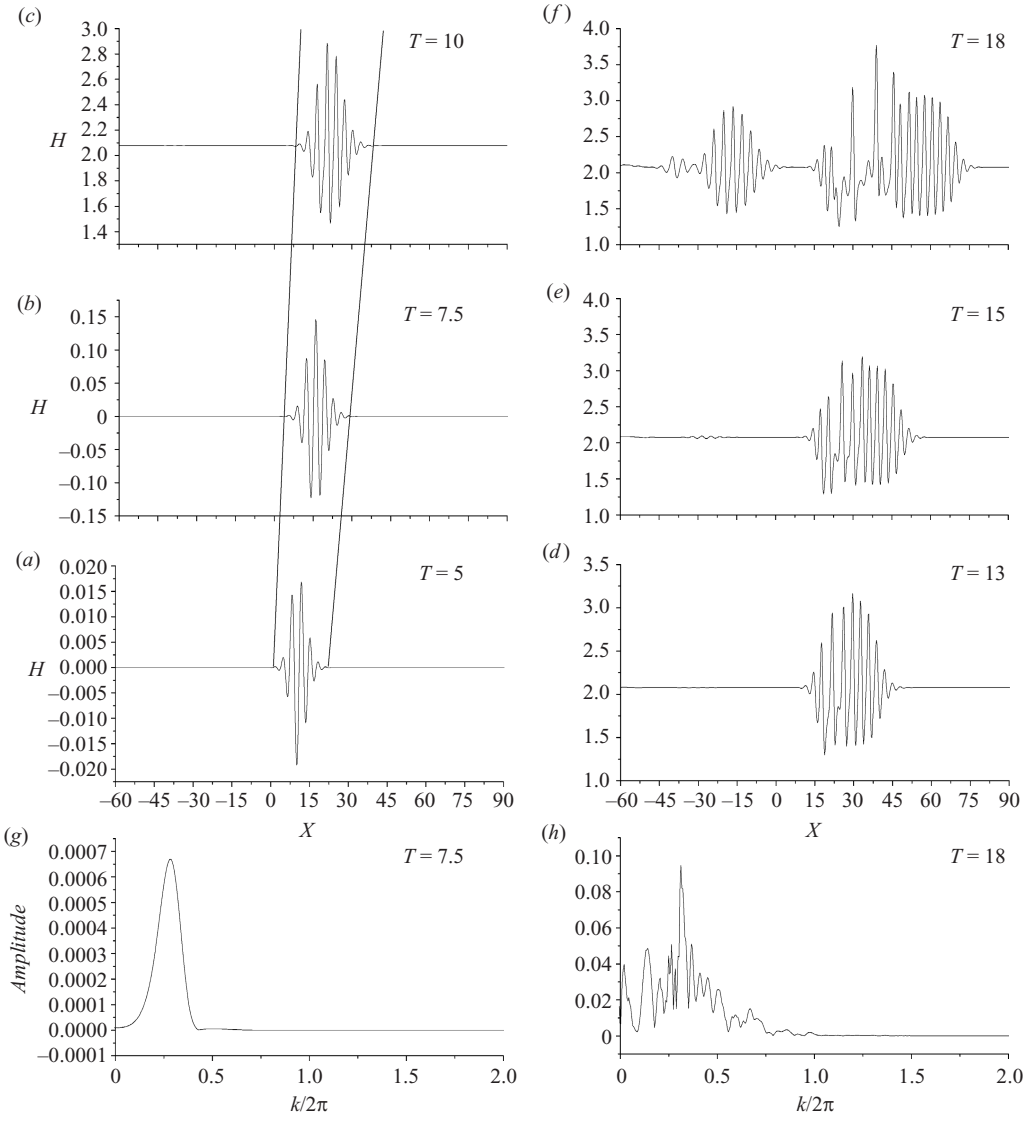


FIGURE 8. Snap-shots: (*a*)–(*f*) and FT (*g*), (*h*) of the interfacial waves for the air deicing system in response to an impulsive disturbance; $H_0 = 2.07$, $d = 0.001$, $x = 0.8$.

out that results on wave packet spread and growth and spike formation, for long time after imposition of an initial disturbance of small amplitude or relatively early for large amplitudes, had to be obtained by carrying out simulations over a very long interval in the longitudinal direction. This was necessary in order to accommodate the forerunning waves along with the ones emerging later on in time. Thus a large number of elements had to be utilized in the simulations with a uniform mesh, e.g. 800 elements when a total of 200 units in the longitudinal coordinate X were necessary for capturing the film dynamics (figures 8 and 12). Employing the adaptive mesh option afforded very accurate results with as many as 400 elements for the same simulations, figure 14, thus confirming the effectiveness of 'packing' the elements in regions exhibiting large variation of the interfacial position.

https://doi.org/10.1017/S0022112009990644 Published online by Cambridge University Press

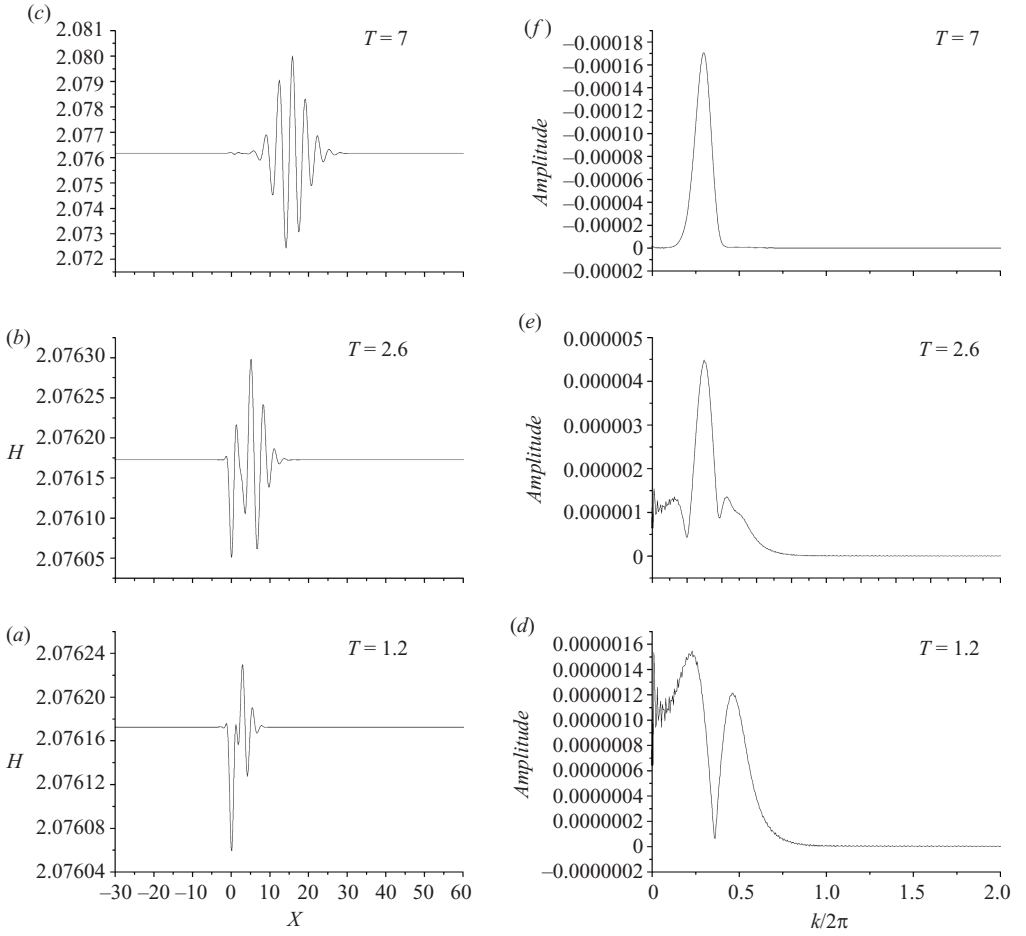


FIGURE 9. Snap-shots: (*a*)–(*c*) and FT (*d*)–(*f*) of the interfacial position for the case of air deicing system in response to a time periodic disturbance; $\omega_f = 9$, $H_0 = 2.076$, $d = 0.001$ and $x_0 = 0.8$.

Applying a disturbance that is local in space but sinusoidal in time (defined in (2.14*b*)), we simulate the 'signalling' problem. Owing to the convectively unstable nature of the flow we expect that as time increases, provided that ω_f lies in the unstable region in the frequency spectrum, behind the advancing wave packet of unstable waves a train of spatially growing waves will be established characterized by a wavelength k_f that corresponds to the imposed frequency ω_f (Huerre & Monkewitz 1990). Figure 9 depicts the evolution of the interface at three different time instants for such a disturbance; $d = 0.001$, $\omega_f = 9$, $H_0 = 2.076$ and $x_0 = 0.8$. The FT of the interface indicates the emergence of an additional length scale. The latter corresponds to the most unstable wave whereas the former is directly related to the forcing frequency. The motion of the dominant wave packet, superimposed on the spatially growing mode, is clearly shown in the panels of figure 9. After an initial transient during which both modes coexist, the most unstable mode grows and eventually dominates the dynamics. Thus, as time advances, one needs to focus on the region behind the wave packet in order to identify the wavelength k_f provided by spatial stability

https://doi.org/10.1017/S0022112009990644 Published online by Cambridge University Press

	Linear theory without film inertia	Linear theory with film inertia	Numerical results without film inertia	Numerical results with film inertia
Wavelength	4.8	3.85	4.87	3.9
Period	2	3.1	2.05	3
Group velocity	3	1.5	3.1	1.45

TABLE 5. Most unstable wave characteristics for interfacial waves of the air–water system predicted analytically and computed numerically with the two different models, with and without inertia effects; $x_0 = 1.5$, $H_0 = 3.32$.

analysis. The FT panels, shown in figure 9, clearly illustrate this behaviour. More details on the nonlinear evolution of such waves are provided in the next subsection.

We then reexamine the case of deicing fluid presented above, including the effect of inertia in the film in order to assess its influence on the evolution of interfacial waves. We introduce the same disturbance as in the case without inertia depicted in figure 8, and numerically follow the spatiotemporal evolution of the wave. The characteristics of the most unstable wave are recovered and compared against the findings of linear theory and numerical simulations without inertia effects (table 4). Both models provide the same values for the wavelength frequency and group velocity of the most unstable wave, as expected due to the very small value of $\mathfrak{M} \approx 10^{-9}$. Therefore the model that neglects film inertia is sufficient to describe the dynamic behaviour of this particular system.

Next we consider the case of a water film, also in the limit of negligible inertia, despite the fact that in this case the ratio of viscosities is not too small, $\mathfrak{M} \approx 0.3$. We introduce an impulsive linear disturbance, $H_0 = 3.32$, $x_0 = 1.5$ and $d = 0.0001$, and calculate the characteristics of the resulting wave. According to linear theory, in the limit of negligible inertia effects, the water–air system is convectively unstable for disturbances at position ranging up to $x_0 = 1.2$. Beyond this critical location a region of absolute instability exists. This is indeed verified by the simulations whereby the numerical period, wavelength and group velocity of the most unstable wave are found to be 2.05, 4.87 and 3.1 respectively, in agreement with the predictions of linear stability analysis for this case (table 5). It should also be pointed out that the selection criterion for global instability (Chomaz, Huerre & Redekopp 1991) also applies for the water–air system without film-inertia,

$$\frac{\partial \omega}{\partial k}\left(k, x; \overline{We}, \overline{Fr}\right) = \frac{\partial \omega}{\partial x}\left(k, x; \overline{We}, \overline{Fr}\right) = 0, \quad \omega = \omega\left(k, x; \overline{We}, \overline{Fr}\right) \tag{4.2}$$

with k, ω and x taken to be complex variables, and assuming a constant rainfall rate for the base state (defined in (2.1a)). The analysis is performed on dispersion relation (4.1) and the growth rate of the global mode frequency ω_G turns out to be quite small, $\omega_{Gi} \approx 0.02$. The effect of nonlinearity on the relative importance of absolute and convectively instabilities as well as the possibility for a global mode to arise is investigated in the next subsection.

We then repeat the investigation of the air–water system, subject to the same type of disturbance, with the model that accounts for film inertia. It is important to mention that for this particular case linear theory predicts absolute instability when $0.8 \leqslant x_0 \leqslant 3$. Figure 10 depicts the evolution of the interface with time along with its FT at a selected time instant for an impulsive disturbance at $x_0 = 1.5$, revealing the onset and translation of the growing wave packet. It is characterized by a significant reduction of the group velocity as well as of the wavelength of the most dangerous

https://doi.org/10.1017/S0022112009990644 Published online by Cambridge University Press

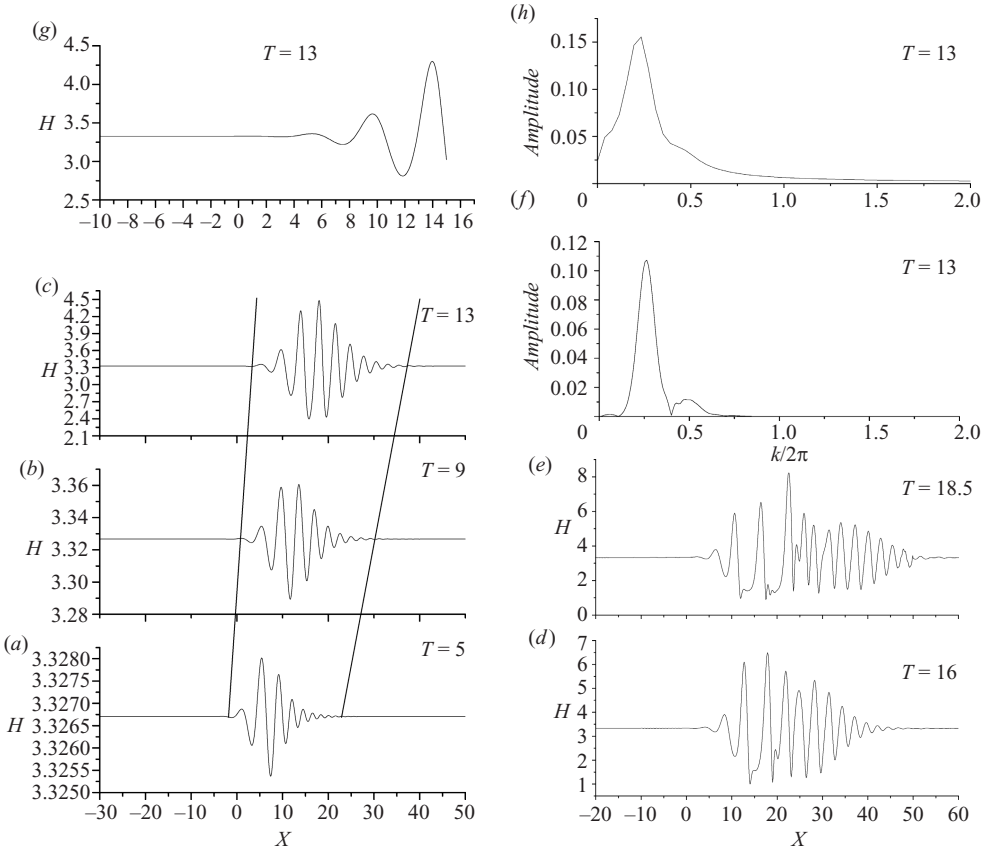


FIGURE 10. Snap-shots of the interface: (*a*)–(*e*) FT of the interface over the entire computational domain at time $T = 13$, (*f*) shape of the interface around position $X = 0$ at $T = 13$, (*g*) FT of the interface around position $X = 0$ at time $T = 13$ (*h*). The case of air–water system is considered when inertia is accounted for in response to an impulsive disturbance; $H_0 = 3.326$, $d = 0.0001$ and $x_0 = 1.5$.

wave as a result of increased inertia. Thus, the shape of the interface is clearly dominated by the most unstable wave.

By performing an FT on the numerical results, figure 10(*f*) we find that the fastest growing wave has a wavelength equal to 3.9 instead of 4.8 predicted in the absence of inertia. Moreover, the group velocity is found to be on the order of 1.5 instead of 3. The above findings are in agreement with the predictions of linear stability analysis when inertia forces of the film are included (table 5). The wavelength of the absolutely unstable mode, $2\pi/k_0 = 4.45$, is only identifiable if one focuses in the region around the origin (figure 10*h*). This is clearly illustrated in figure 10 depicting the shape of the interface throughout the computational domain and in a region near the origin at $T = 13$ (figures 10*c* and 10*g*) and their respective FT (figures 10*f* and 10*h*). In fact, the absolutely unstable mode progressively becomes less and less identifiable as it is dominated by the most unstable wave. This is partially understood in the light of linear theory since the growth rate of the absolutely unstable mode, $\omega_{0i} \approx 0.09$, is much smaller than the growth rate of the most unstable wave, $\omega_i = 0.78$. Consequently, the wave with vanishing group velocity occupies the left region of the wave packet which essentially never entirely leaves the position of the initial disturbance. It should be stressed that the amplitudes shown in figures 10(*f*) and 10(*h*) are scaled and

https://doi.org/10.1017/S0022112009990644 Published online by Cambridge University Press

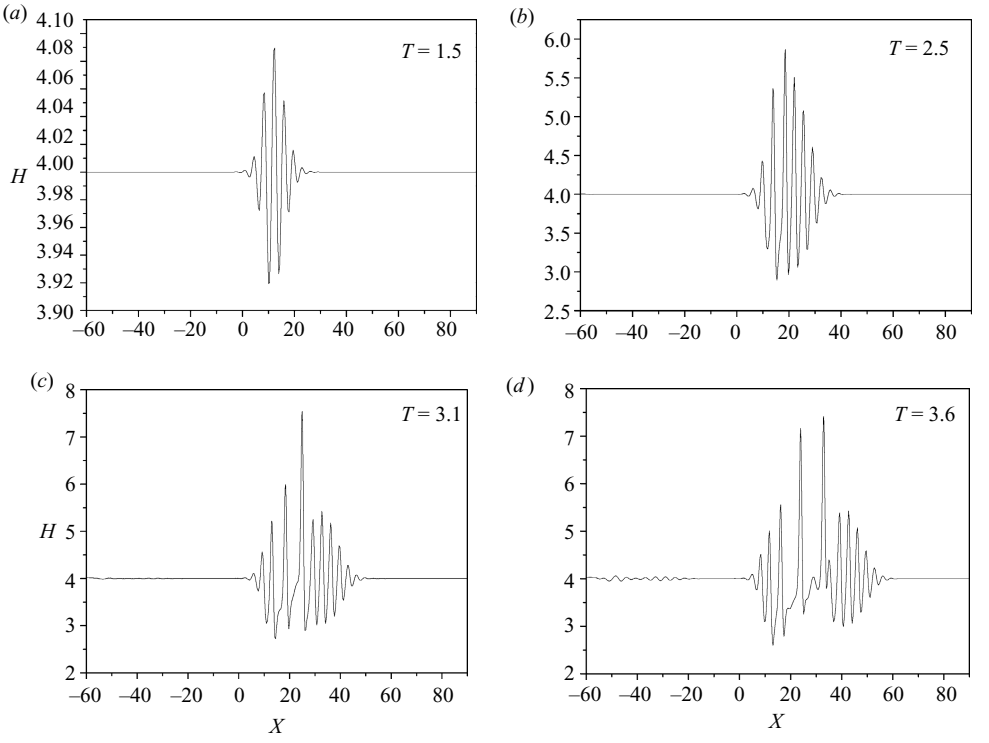


FIGURE 11. Snap-shots: (*a*)–(*d*) of the interfacial position for the case of air deicing system, in response to an impulsive disturbance; $H_0 = 4$, $d = 0.001$ and $x_0 = 0.8$.

consequently they should not be compared. Rather, the wavenumbers corresponding to amplitude maxima are of interest as they provide the relevant wavelength, $\ell = 2\pi/k$.

4.2.2. *Results for interfacial waves in the nonlinear regime*

The above discussion has shown that our numerical approach can adequately capture growth of interfacial waves in the presence of a boundary layer, in the linear regime. We now proceed in examining the effect of nonlinearity on film growth. To this end, we either impose an initial disturbance that is characterized by larger amplitude or run the simulations over a longer time interval. In both cases we expect to get a more realistic view on the actual film dynamics.

We first focus on the case of a film of deicing fluid that is depicted in figure 8 and register the shape of the interface as time increases beyond the range of validity of linear theory. As illustrated by the panels of figure 8 showing the location of the interface, the wave packet predicted by linear theory becomes flatter indicating a tendency to generate a wavetrain dominated by the wavelength of the most unstable wave. However, in this process the waves forming the wave packet become unstable and the latter disintegrates to a rather irregular wave structure that is characterized by spikes. It is important to note that the height of such structures can be as large as twice the original film height and it was not seen to exceed that height in any of the simulations that we carried out. Figure 11 shows the evolution of a deicing film with initial dimensionless thickness $H_0 = 4$ subject to the same type of disturbance as in figure 8. Indeed the dynamics of film growth is very similar with those portrayed in figure 8, with the emerging spikes appearing over the same time scale while reaching

https://doi.org/10.1017/S0022112009990644 Published online by Cambridge University Press

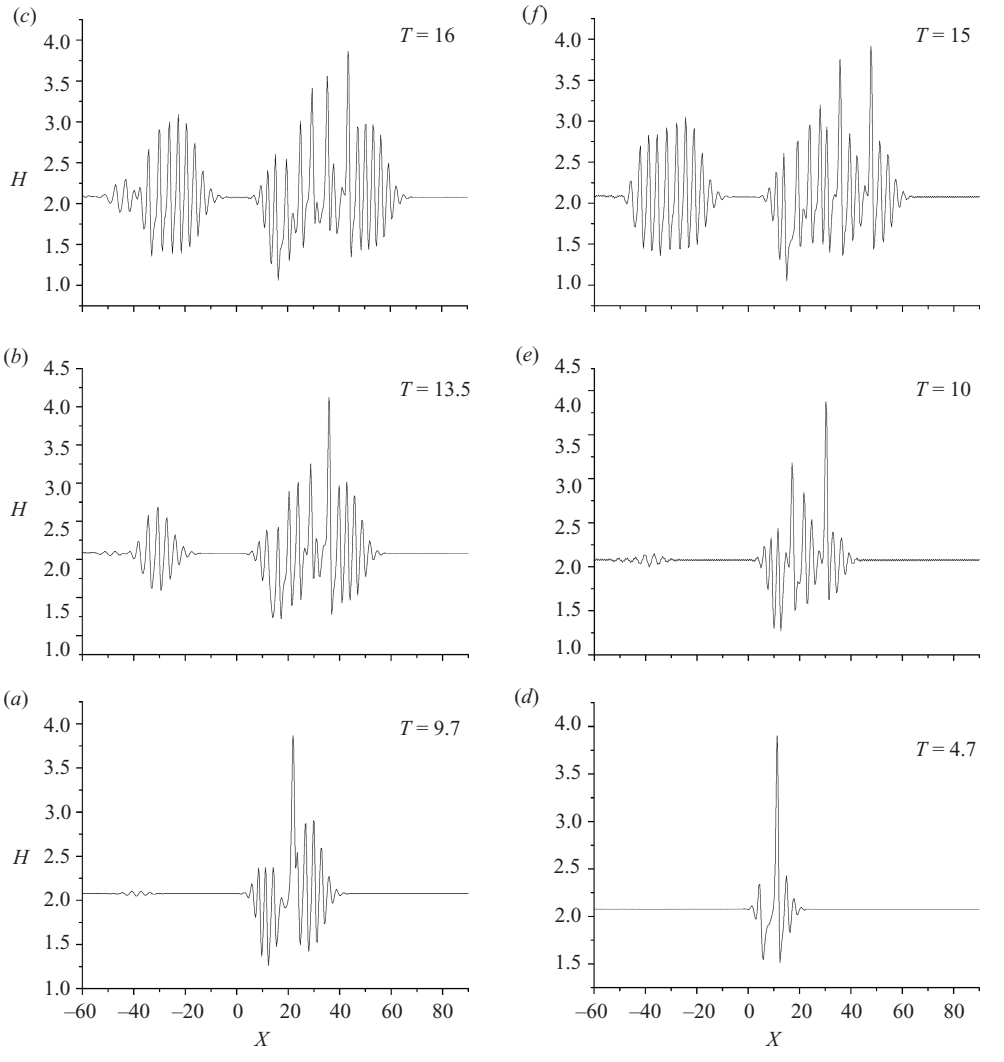


FIGURE 12. Snap-shots of the interfacial waves for the air deicing system in response to an impulsive disturbance, $H_0 = 2.076$ and $x = 0.8$, when (a), (b) and (c) $d = 0.2$ and (d), (e) and (f) $d = 0.4$.

twice the initial film height. Increasing the initial disturbance to $d = 0.2$ and 0.4 and repeating the simulation we recover the above pattern, only at a shorter time interval, of wave packet flattening and destabilization into a succession of spikes that reach twice the initial film height, figure 12. The spikes again move at a speed that is larger than that of the original linear waves, $u_g = 3.75$; their wavelength is longer and their rate of appearance indicates that there is a tendency of such longer waves to progressively dominate the shape of the interface. In fact beyond a certain range in the amplitude of the disturbance the linear part of the evolution of the wave packet is no longer obtained as it is rapidly bypassed by spike formation.

As can be surmised by the shape of the interface around the spikes, they are forerun by a series of short wavelength and much smaller height capillary waves while they are followed by a region of relatively uniform height. This structure is reminiscent of

https://doi.org/10.1017/S0022112009990644 Published online by Cambridge University Press

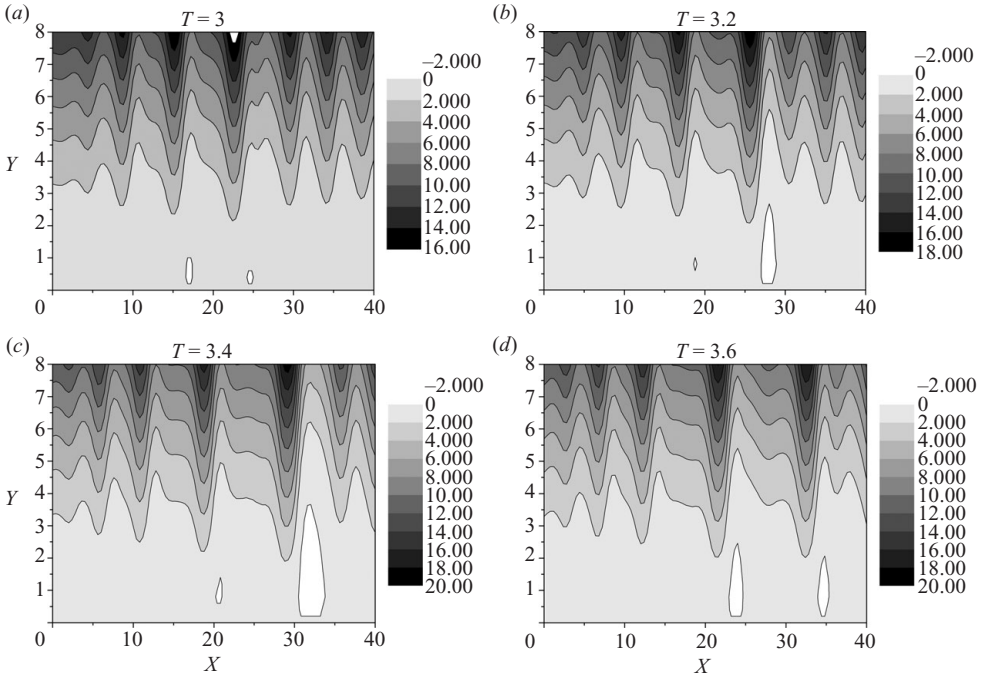


FIGURE 13. Evolution of the streamfunction for the air deicing system in response to an impulsive disturbance; $H_0 = 4$ and $d = 0.001$.

solitons that tend to appear when long waves dominate water waves. The intensity of the above capillary waves is dependent on the relative importance of capillarity and film inertia as they are characterized via $\overline{We}$ and film Reynolds,

$$Re_f = \frac{\rho_w u_f H_f}{\mu_w} \approx \frac{\rho_w \left(\lambda H_0 \frac{\mu}{\mu_w} U_\infty Re^{-1/8}\right)\left(H_0 L Re^{-5/8}\right)}{\mu_w} = \lambda H_0^2 \frac{\nu \rho_w \mu}{\mu_w^2} Re^{2/8} = \lambda H_0^2 Re^{2/8}. \tag{4.3}$$

Upon comparing spike formation illustrated in figures 8(f) and 11(d) one notices that a larger base flow film thickness H_0, eventually leads to a weaker capillary wave formation downstream of the spike. Increasing the amplitude of the initial disturbance in the shape of the film also amounts to increasing film inertia. This is clearly manifested in the progressively weaker capillary activity ahead of the dominant spikes exhibited in figures 8(f), 12(c) and 12(f), corresponding to amplitudes $d = 0.001$, 0.2 and 0.4. Figure 12(d–f), pertaining to the largest amplitude $d = 0.4$, clearly illustrate the formation of a similar second spike following the leading one indicating the pattern of soliton formation. The speed of the spike was also calculated and the tendency for higher speed with increasing spike height was verified. Similar effects and their association with the film Reynolds were observed experimentally and analysed numerically in a recent article on soliton formation in vertically falling films (Meza & Balakotaiah 2008).

Figure 13 depicts the evolution of streamfunction in the gas phase near the interface for the flow situation of figure 11. Areas of mild flow recirculation are clearly indicated by white colour regions where streamfunction is negative; the streamfunction of the gas phase vanishes exactly on the interface. They are located just ahead of the spikes

https://doi.org/10.1017/S0022112009990644 Published online by Cambridge University Press

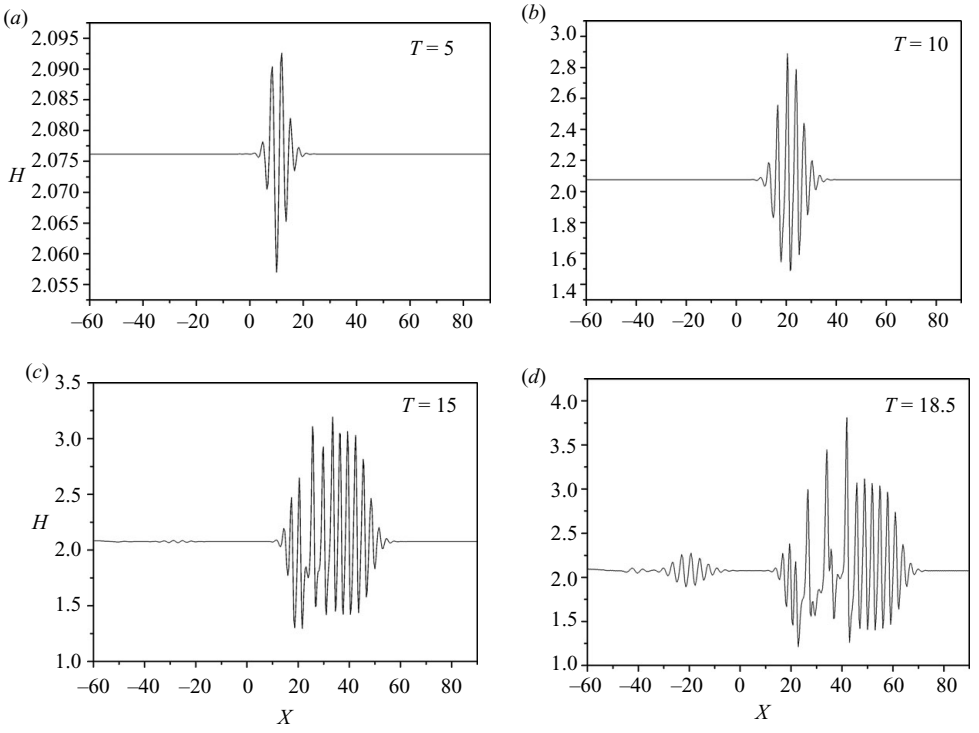


FIGURE 14. Snap-shots of the interfacial waves for the air deicing system in response to an impulsive disturbance using a total of 400 elements in the longitudinal direction combined with the adaptive mesh option; $H_0 = 2.076$, $d = 0.001$ and $x = 0.8$ as in figure 8.

and they periodically come and go following the slight fluctuation of the height of the spikes. The same behaviour is recovered in the case of a time periodic disturbance at long times after the imposition of the initial disturbance, figure 9. The most unstable wave evolves in the fashion described above, whereas the spatially growing wave is rapidly modified as it interacts with the wave packet that spreads out as it is convected downstream. Spike formation is again the dominant long-time behaviour.

We now proceed to examine how nonlinearity affects the air–water system and thus to determine the role of inertia in the nonlinear regime. To this end, we focus on the simulation for boundary layer flow over a water film and we either follow the linearly excited interfacial wave over a longer time interval or we set a greater initial disturbance. The flow arrangement presented in figure 10 for a disturbance with $d = 0.0001$ at $X_0 = 1.5$ is followed over a longer period of time. As can be gleaned from the corresponding panels of figure 10 the shape of the interface exhibits a much different behaviour than the one observed for the air deicing system. When inertia of the liquid is taken into consideration the shape of the interface is dominated by a single spike. Moreover, the height of the emerging spike is more than double the initial film height and there is no indication that it will stop growing beyond a certain value. In addition, upstream of the maximum spike we observe an area of film depletion. The wavelength corresponding to the absolutely growing mode is not identified in the FT plot covering the entire computational domain, figure 10(*f*), as it is dominated by the most unstable wave, that constantly grows and spreads over large portions of the flow domain, and its harmonics. The onset of a frontal arrangement of the travelling

https://doi.org/10.1017/S0022112009990644 Published online by Cambridge University Press

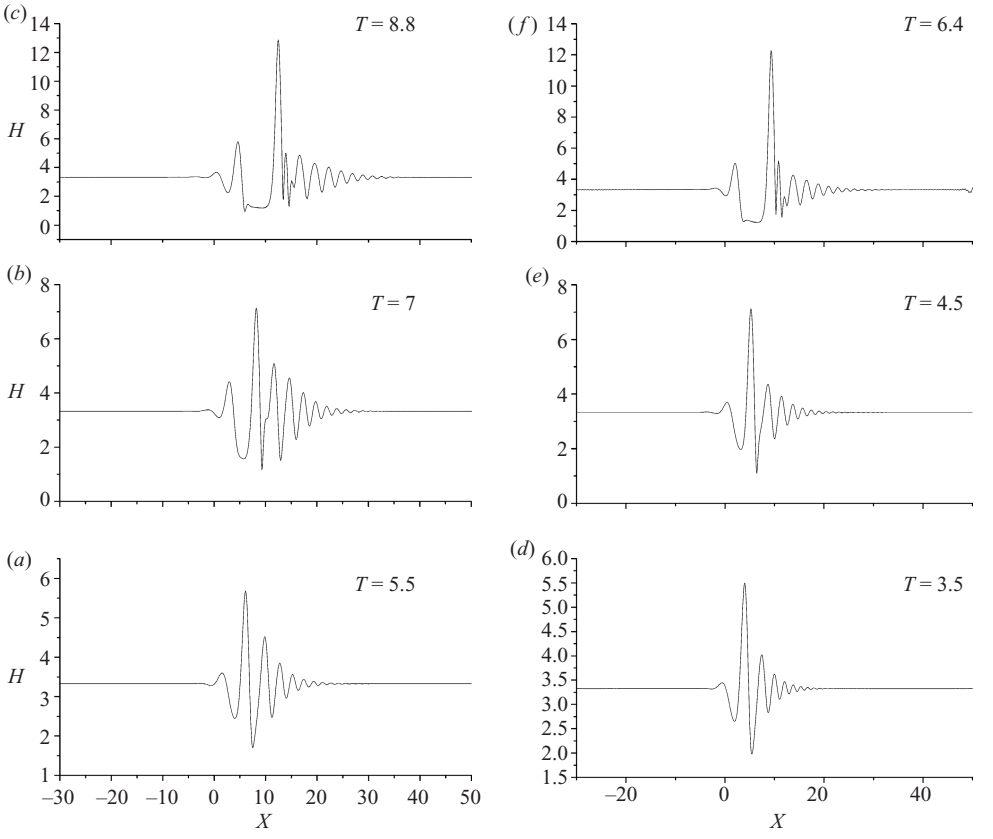


FIGURE 15. Snap-shots of the interfacial waves for the air–water system in response to an impulsive disturbance, $H_0 = 3.326$ and $x = 1.5$, when (*a*), (*b*) and (*c*) $d = 0.1$ and (*d*), (*e*) and (*f*) $d = 0.4$.

wave packet is not observed in figure 10 as the wave packet never reaches saturation due to spike formation. Repeating the simulation with a larger initial disturbance recovers the above pattern at a shorter time scale (figure 15). In fact, as the amplitude increases significantly, $d = 0.4$, the linear part of the evolution of the wave packet is bypassed and spike formation is evident almost immediately after imposition of the disturbance. The streamline pattern for the case with $d = 0.1$ is shown in figure 16 indicating areas of intense recirculation in white colour ahead of the emerging spike. The height and thickness of the flow reversal region is growing in response to the developing spike which acts as a sink of the surrounding liquid. Thus, the effect of inertia in the case of the air–water system is to generate a single structure of large thickness that blocks the flow of the surrounding gas leading to large pressure drops (figure 17) and significant flow reversal.

An interesting issue regarding the evolution of interfacial waves is the possibility for a global instability to arise when longitudinal variations in the base flow are taken into account. Indeed, as was seen in the previous subsection, the criterion for global instability is satisfied for the air–water system in the absence of inertia effects, whereas there is evidence that it is present even when inertia effects are accounted for since there is an interval in x within which the flow is absolutely unstable (Pelekasis & Tsamopoulos 2001). Simulations were carried out for both situations, allowing for

https://doi.org/10.1017/S0022112009990644 Published online by Cambridge University Press

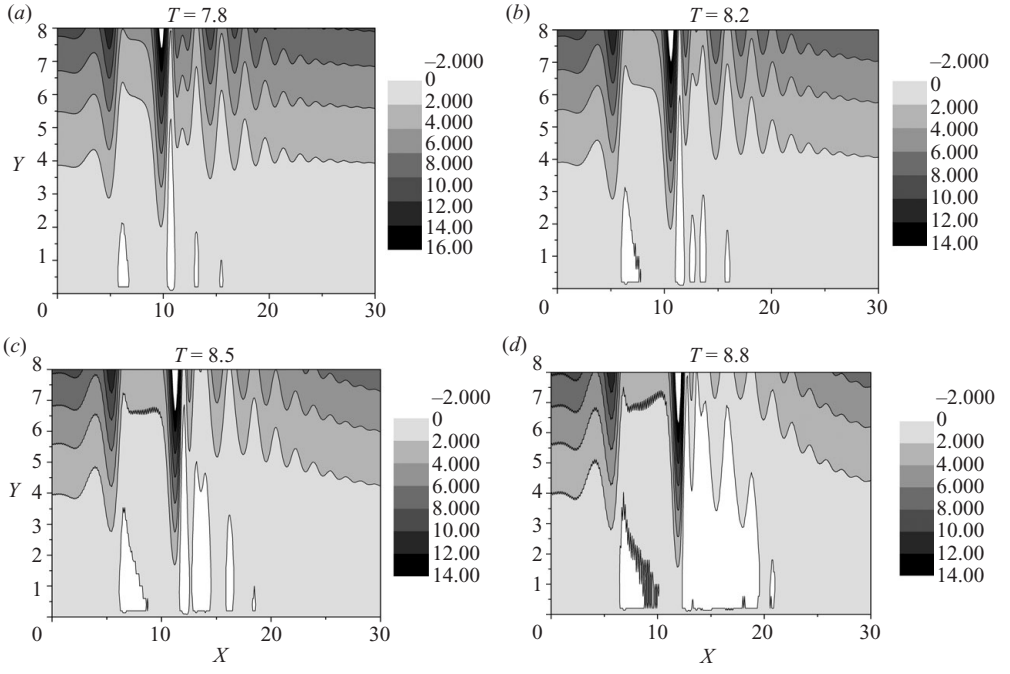


FIGURE 16. Evolution of the streamfunction for the air–water system in response to an impulsive disturbance; $H_0 = 3.326$ and $d = 0.1$.

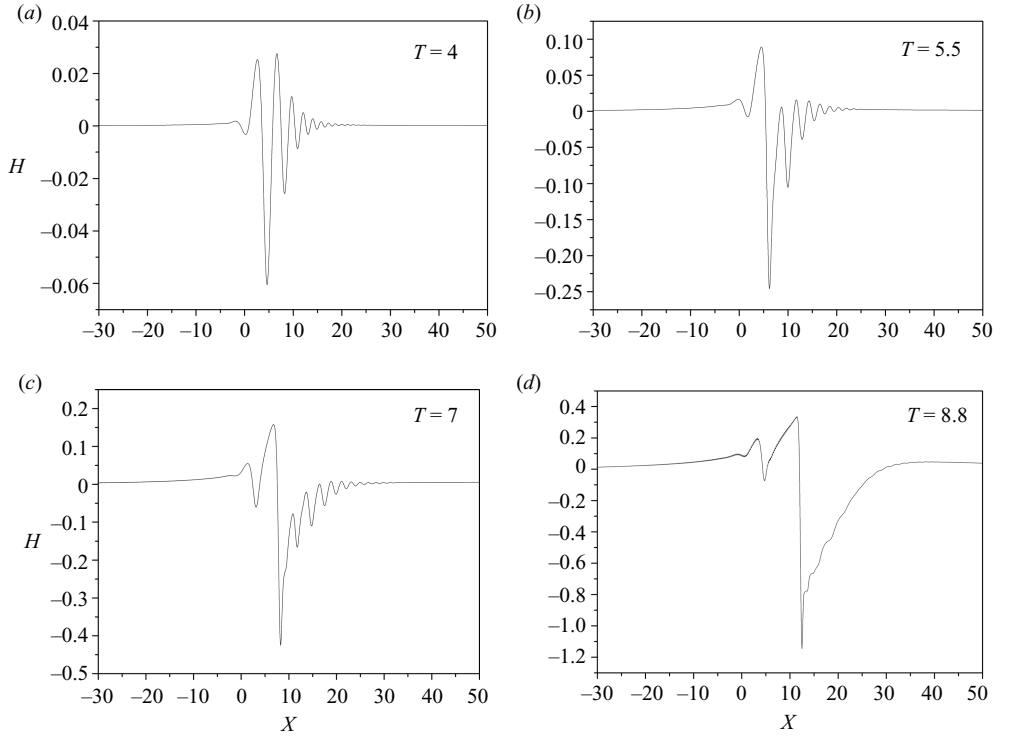


FIGURE 17. Spatiotemporal evolution of pressure for the air–water system with initial height 3.326 and $d = 0.1$.

https://doi.org/10.1017/S0022112009990644 Published online by Cambridge University Press

Deicing fluid	ρ/ρ_w	μ/μ_w	$\mathfrak{M}$	$\overline{Fr}$	$\overline{We}$
M75 (25% water)	0.00131	1.22×10^{-3}	0.00114	39425.148	58.63
M50 (60% water)	0.00132	2.83×10^{-3}	0.006	39425.15	65.81
D100 (neat)	0.00128	9.38×10^{-4}	0.00068	39425.155	47.37
D75 (25% water)	0.001	1.98×10^{-3}	0.0039	39425.13	59.38

TABLE 6. Dimensionless parameters for different deicing fluids.

the film thickness and shear to vary as prescribed by (2.1) and the Blasius solution, respectively, and setting Re to 10^5 in order to calculate x when X varies along the computational domain with $X=0$ corresponding to x_0. $x_0=1.5$ was chosen for the case with inertia effects included. This value corresponds to the highest growth rate of the absolutely unstable mode in the range of absolute instability, $0.7 \leqslant x \leqslant 3$. The evolution of the interface in the latter flow situation, the case with the air–water system without inertia effects behaving quite similarly, indicated that the structure with the growing spike still dominates the system dynamics. The only difference between the interfacial shape as obtained in this fashion and the one in figure 15 where uniform initial film thickness and film velocity are assumed, lies in the weak variation of film thickness with X underneath the fast variation of the evolving wave packet.

These findings are in agreement with the experimental observations of Craik (1966) who studied the waves that develop in the air–water interface for thin liquid films and large Re. Craik (1966) conducted experiments in a channel and was able to capture 'slow' waves with a propagation speed smaller than or of the same order of magnitude as the velocity of the liquid surface. In the same study he reported that these waves are non-periodic and as they evolve they form steep spikes with height that significantly exceeds the mean thickness value. He also reported dry regions of very small film thickness as the average film thickness decreased. In our simulations the dimensionless speed of wave propagation is estimated to be 1.1 while the velocity of the surface is equal to 0.77 for the air–water system, which is of the same order of magnitude. Despite the fact that in the present study air flow is in the form of a laminar boundary layer rather than turbulent Poiseuille flow, as is the case in Craik's experiments (Craik 1966), the small film thickness guarantees that air-film interaction is within the laminar sublayer in which case the bulk of the analysis employed here is valid. Based on the above, we conjecture that the interfacial waves captured here are the 'slow' waves according to Craik's definition.

Having established the significant role that film inertia plays on the evolution of interfacial waves, we then try to determine the minimum value of parameter $\mathfrak{M}$ above which inertia plays an important role. We use four different deicing fluids with properties that are provided by Ozgen, Carbonaro & Sarma (2002). Furthermore, we assume the same chord length, air velocity, shear and initial film height as in the case of the deicing fluid examined previously ($L=0.279$ m, $U_\infty=27.28$ m s^{-1}, $\lambda=0.371$, $H_0=2.076$). Table 6 gives the relevant dimensionless parameters that are used in the computations while figure 18 illustrates the long-time behaviour of the interface for each case. As one can easily glean from figure 18 only deicing fluid M50 forms a peak of continuously increasing height that does not have the tendency to saturate. The rest of the fluids appear to follow the behaviour observed for liquids with large viscosity where the disturbance reaches a certain maximum height and stops growing

https://doi.org/10.1017/S0022112009990644 Published online by Cambridge University Press

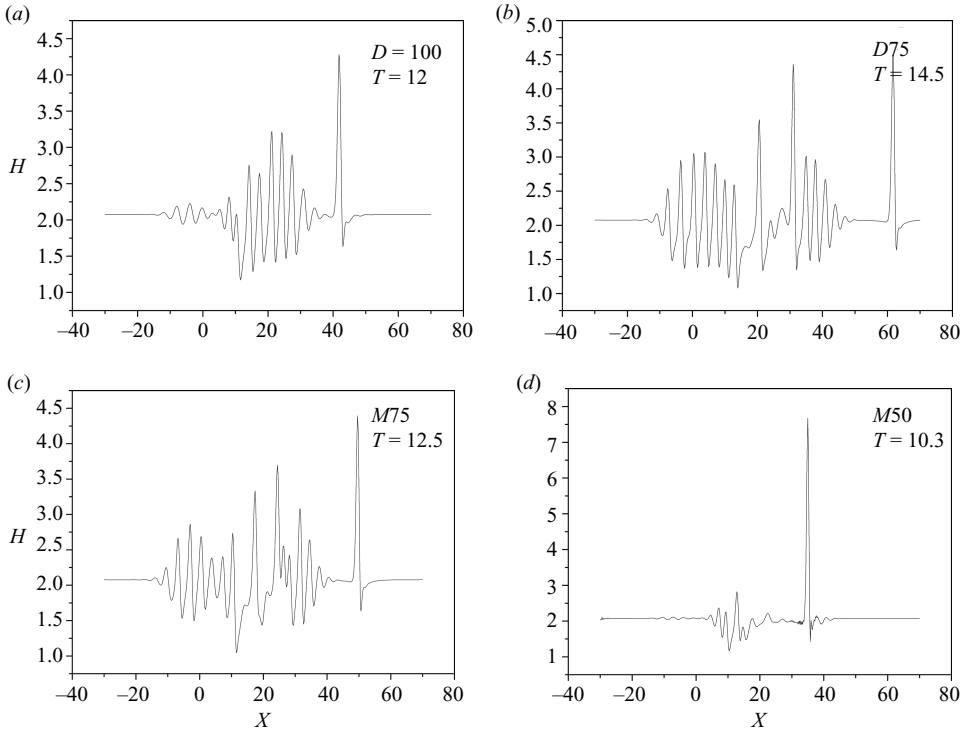


FIGURE 18. Snapshots of the interface long-time behaviour for four different deicing fluids when inertia of the film is included: (*a*) M75, (*b*) M50, (*c*) D100 and (*d*) D75.

any further. This behaviour is correlated with the value of parameter $\mathfrak{M}$ of the above fluids. Indeed deicing fluid M50 has the largest $\mathfrak{M}$ value among them, 0.006. Thus we can conclude that for given initial height and shear there is a minimum value of parameter $\mathfrak{M}$ above which film inertia modifies the flow pattern leading to an intense recirculation pattern. In the context of vertically falling films it was seen by Meza & Balakotaiah (2008) that as the effect of film viscosity is decreased film height tended to saturate to a much larger thickness. In the present study severely increased film thicknesses should be compensated by a much larger displacement thickness for the boundary layer and a significantly larger computational domain in the transverse direction, $\bar{Y}_\infty$. However, as the film thickness increases dramatically and massive separation takes place the triple-deck structure loses validity and a different approach should be adopted. Hence a more comprehensive investigation for a saturation height of the spikes when film inertia is important was not pursued in the present study.

The evolution of pressure distribution and the streamline pattern, illustrated in figures 17 and 16 for the air–water system, indicate the tendency towards formation of a finite time singularity leading to breakup of the boundary layer formulation during the last stages of the simulations. This process occurs in the manner described by Smith (1988) via a singularity in the pressure distribution. The pressure distribution and streamline pattern are similar to the numerical predictions by Peridier *et al.* (1991*b*) for the case of a vortex that interacts with a boundary layer over a plate. It is interesting to note that in the present study the boundary layer is taken to be quasi-steady and consequently the process in instigated by unlimited growth of interfacial waves. This attests to the universality of the process of singularity formation, since

https://doi.org/10.1017/S0022112009990644 Published online by Cambridge University Press

TS waves do not play a role in the simulations discussed in §4.2, in the unsteady interactive boundary layer formulation. It should also be stressed that the air deicing fluid flow system does not exhibit such an unlimited growth and finite time singularity formation. Rather, it tends to saturate once the spikes achieve a certain average height. This is a result of the diminishing effect of film inertia for such ultra-high viscosity films. A very small base flow film thickness or shear rate, amount to loss of film inertia leading to height saturation as well. Consequently, it can be argued that viscous effects can negate the process of singularity formation and saturate the film thickness. A similar outcome in the balance between inertia and viscosity is observed in finite time singularity formation in the context of bubble oscillations and breakup (Tsiglifis & Pelekasis 2005). The balance between inertia and capillarity determine the time and space scales for the pinching process of a sufficiently elongated bubble of initial radius R, via a finite time singularity. When viscous effects are accounted for there is a threshold in Ohnesorge number, $Oh = \mu/(\rho R\sigma)$ that compares the relative importance of viscous and capillary forces, below which pinching does not take place and the bubble finally returns to its initial spherical shape.

5. Conclusions

Concluding we should stress the success of B-cubic splines within the context of the finite element methodology, in capturing severe interfacial wave phenomena due to their increased accuracy and smoothness. Their superiority over conventional Lagrangian basis functions is also notable and worth being explored in more general flow arrangements, perhaps even for the solution of the full Navier–Stokes equations combined with the appropriate 'staggered grid' formulation for pressure. The latter might be in the form of a spline representation of lower accuracy than cubic. Regarding the problem under investigation, it is important to point out the splitting of time scales for most common air–liquid systems characterized by very small viscosity ratio, $\mu/\mu_w \to 0$. Assuming a quasi-steady state for the gas simplifies the problem significantly and allows for capturing interfacial phenomena that occur on a much slower time scale than the passage of TS waves. The effect of wavelengths pertaining to interfacial waves, which are smaller than those corresponding to classical TS waves, in bypassing transition is also identified in simulations of the full gas–liquid interaction problem. Focusing on interfacial wave growth, the results of linear theory are captured but they are seen not to be able to describe long-time or large-amplitude system dynamics. In fact, very viscous liquids where film inertia is negligible evolve into longer waves that are characterized by spikes that travel much faster than the original wave packets predicted by linear theory. A number of such waves are observed whose structure and speed resemble solitons that only grow up to a certain height that is, roughly, twice the initial film thickness. When film inertia is important the spike structure is replaced by a single spike that is constantly growing, followed by a region of film depletion. Ahead of the spike a region of intense recirculation is captured that ultimately leads to massive boundary layer separation. The mechanics of this process are attributed to the formation of a finite time singularity in the pressure distribution in a manner that is universal for the unsteady interacting boundary layer formulation, irrespective of its association to TS or interfacial waves. In the case of air deicing fluids excessive film viscosity inhibits the development of singularities leading to saturated spike formation. The repercussions of these effects in the aerodynamic characteristics of airfoils under conditions of rainfall are obvious and deserve further

https://doi.org/10.1017/S0022112009990644 Published online by Cambridge University Press

investigation in order to verify whether such a behaviour persists in the presence of other hydrodynamic effects, e.g. onset of three-dimensional disturbances.

Ms Maria Vlachomitrou wishes to acknowledge the scholarships 'PENED' of the Greek Secretariat of Research and 'PYTHAGORAS' of the Greek Ministry of Education, for support during this work. Discussions with Dr D. Smyrnaios on the numerical implementation of two-dimensional B-cubic splines are greatly appreciated.

REFERENCES

Bezos, G. M., Dunham, R. E., Gentry, Jr. G. L. & Melson, W. E. 1992 Wind tunnel aerodynamic characteristics of a transport-type airfoil in a simulated heavy rain environment. *Tech Rep.* TP-3184. NASA.

Bowles, R., Davies, C. & Smith, F. T. 2003 On the spiking stages in deep transition and unsteady separation. *J. Engng Math.* **45**, 227–245.

Brotherton-Ratcliffe, R. V. & Smith, F. T. 1987 Complete breakdown of an unsteady interactive boundary layer (over a surface distortion or in a liquid layer). *Mathematica* **34**, 86–100.

Caponi, E. A., Fornberg, B., Knight, D. D., Mclean, J. W., Saffman, P. G. & Yuen, H. C. 1982 Calculations of laminar viscous flow over a moving wavy surface. *J. Fluid Mech.* **124**, 347–362.

Cassel, K. W., Ruban, A. I. & Walker, D. A. 1995 An instability in supersonic boundary-layer flow over a compression ramp. *J. Fluid Mech.* **300**, 265–285.

Cassel, K. W., Ruban, A. I. & Walker, D. A. 1996 The influence of wall cooling on hypersonic boundary-layer separation and stability. *J. Fluid Mech.* **321**, 189–216.

Chomaz, J. M., Huerre, P. & Redekopp, L. G. 1991 A frequency selection criterion in spatially developing flows. *Stud. Appl. Math.* **84**, 119–144.

Craik, A. D. D. 1966 Wind generated waves in thin liquid films. *J. Fluid Mech.* **26** (2), 369–392.

De Boor, C. 1978 *A Practical Guide to Splines*. Springer.

Duck, P. W. 1985 Laminar flow over unsteady humps: the formation of waves. *J. Fluid Mech.* **160**, 465–498.

Elliott, J. W., Cowley, S. J. & Smith, F. T. 1983 Breakdown of boundary layers: (i) on moving surfaces; (ii) in self-similar unsteady flow; (iii) in fully unsteady flow. *Geophys. Astrophys. Fluid Dyn.* **25**, 77–138.

Fletcher, A. J. P., Ruban, A. I. & Walker, J. D. A. 2004 Instabilities in supersonic compression ramp flow. *J. Fluid Mech.* **517**, 309–330.

Gresho, P. M. & Sani, R. L. 1998 *Incompressible Flow and the Finite Element Method: Volume II*. Wiley.

Hendrickson, G. S. & Hill, E. G. *Effects of aircraft de-anti-icing fluids on airfoil characteristics*, von Karman Inst. for Fluid Dynamics Lecture Series, *Influence of Environmental factors on aircraft performance*. von Karman Inst. for Fluid Dynamics, Brussels, Belgium, Feb. 16–19, 1987.

Huerre, P. & Monkewitz, P. A. 1990 Local and global instabilities in spatially developing flows. *Annu. Rev. Fluid Mech.* **22**, 473–537.

Jenson, R., Burggraf, O. R. & Rizzetta, D. P. 1975 Asymptotic solution for supersonic viscous flow past a compression corner. *Lecture Notes Phys.* **35**, 218–224.

Lac, E., Barthes-Biesel, D., Pelekasis, N. & Tsamopoulos, J. 2004 Spherical capsules in three-dimensional unbounded Stokes flows: effect of the membrane constitutive law and the onset of buckling. *J. Fluid Mech.* **516**, 303 – 334.

Lin, C. C. 1946 On the stability of two-dimensional parallel flows. Stability in viscous fluid. *Quart. Appl. Math.* **3** (4), 277–301.

Ludwieg, H. & Hornung, H. 1989 The instability of a liquid film on a wall exposed to an airflow. *J. Fluid Mech.* **200**, 217–233.

Meza, C. E. & Balakotaiah, V. 2008 Modeling and experimental studies of large amplitude waves on vertically falling films. *Chem. Engng Sci.* **63**, 4704–4734.

Nelson, J. J., Alving, A. E. & Joseph, D. D. 1995 Boundary layer flow of air over water on a flat plate. *J. Fluid Mech.* **284**, 159–169.

https://doi.org/10.1017/S0022112009990644 Published online by Cambridge University Press

Ozgen, S., Carbonaro, M. & Sarma, G. S. R. 2002 Experimental study of wave characteristics on a thin layer of de/anti-icing fluid. *Phys. Fluids* **14**, 3391–3402.

Ozgen, S., Degrez, G. & Sarma, G. S. R. 1998 Two-fluid boundary layer stability. *Phys. Fluids* **10** (11), 2746–2757.

Pelekasis, N. A. & Tsamopoulos, J. A. 2001 Linear stability analysis of a gas boundary layer flowing past a thin liquid film over a flat plate. *J. Fluid Mech.* **436**, 321–352.

Pelekasis, N. A., Tsamopoulos, J. A. & Manolis, G. D. 1992 A hybrid finite-boundary element method for inviscid flows with free surface. *J. Comput. Phys.* **101** (2), 231–251.

Peridier, V. J., Smith, F. T. & Walker, J. D. A. 1991*a* Vortex-induced boundary-layer separation. Part 1. The unsteady limit problem $\mathrm{Re} \to \infty$. *J. Fluid Mech.* **232**, 99–131.

Peridier, V. J., Smith, F. T. & Walker, J. D. A. 1991*b* Vortex-induced boundary-layer separation. Part 2. Unsteady interacting boundary layer theory. *J. Fluid Mech.* **232**, 133–165.

Prender, P. M. 1989 *Splines and Variational Methods*. John Wiley & Sons.

Purvis, R. & Smith, F. T. 2004 Air–water interactions near droplet impact. *Eur. J. Appl. Math.* **15**, 853–871.

Rothmayer, A. P., Matheis, B. D. & Timoshin, S. N. 2002 Thin liquid films flowing over external aerodynamic surfaces. *J. Engng Math.* **42**, 341–357.

Ruban, A. I. 1978 Numerical solution of the local asymptotic problem of the unsteady separation of a laminar boundary layer in supersonic flow *Comput. Math. Math. Phys.* **18** (5), 175–187.

Ryzhov O. S. & Terent'ev, E. D. 1986 On the transition mode characterizing the triggering of a vibrator in the subsonic boundary layer on a plate. *Prikl. Mat. Mekh., J. Appl. Math. Mech.* (Engl. Transl) **50** (6), 753–762.

Saad, Y. & Schultz, M. H. 1986 GMRES: a generalized minimal residual algorithm for solving nonsymmetric linear systems. *SIAM J. Sci. Stat. Comput.* **7**, 856–869.

Smith, F. T. 1976*a* Flow through constricted or dilated pipes and channels. Part 1. *Quart. J. Mech. Appl. Math* **29** (3), 343–364.

Smith, F. T. 1976*b* Flow through constricted or dilated pipes and channels: Part 2. *Quart. J. Mech. Appl. Math* **29** (3), 365–376.

Smith, F. T. 1979*a* On the non-parallel flow stability of the Blasius boundary layer. *Proc. R. Soc. Lond.* A **366**, 91–109.

Smith, F. T. 1979*b* Nonlinear stability of boundary layers for disturbances of various sizes. *Proc. R. Soc. Lond.* A **368**, 573–589.

Smith, F. T. 1985 A structure for laminar-flow past a bluff body at high Reynolds-number. *J. Fluid Mech.* **155**, 175–191.

Smith, F. T. & Bodonyi, R. J. 1985 On short-scale inviscid instabilities in flow past surface-mounted obstacles and other non-parallel motions. *Aeronaut. J.* **89** (886), 205–212.

Smith, F. T., Brighton, P. W. M., Jackson, P. S. & Hunt, J. C. R. 1981 On boundary-layer flow past two-dimensional obstacles. *J. Fluid Mech.* **113**, 123–152.

Smith, F. T. & Burggraf, O. R. 1985 On the development of large-sized short-scaled disturbances in boundary layers. *Proc. R. Soc. Lond.* A **399**, 25–55.

Smith, F. T. 1986 Two-dimensional disturbance travel, growth and spreading in boundary layers. *J. Fluid Mech.* **169**, 353–377.

Smith, F. T. 1988 Finite time singularity can occur in any unsteady interacting boundary layer. *Mathematica* **35**, 256–273.

Smith, F. T. 1995 On spikes and spots: strongly nonlinear theory and experimental comparisons. *Phil. Trans. R. Soc. Lond.* A. **352**, 405–424.

Smith, F. T., Li, L. & Wu, G. X. 2003 Air cushioning with a lubrication/inviscid balance. *J. Fluid Mech.* **482**, 291–318.

Smyrnaios, D. N., Pelekasis, N. A. & Tsamopoulos, J. A. 2000 Boundary layer flow of air past solid surfaces in the presence of rainfall. *J. Fluid Mech.* **425**, 79–110.

Sychev, VL. V., Ruban, A. I., Sychev, VI. V. & Korolev, G. L. 1998 *Asymptotic theory of separated flows*. Cambridge University Press.

Terent'ev, E. D. 1981 The linear problem of a vibrator in a subsonic boundary layer. *J. Appl. Math. Mech.* **45** (6), 791–795.

Terent'ev, E. D. 1984 The linear problem of a vibrator performing harmonic oscillations at supercritical frequencies in a subsonic boundary layer. *J. Appl. Math. Mech.* **48** (2), 184–191.

https://doi.org/10.1017/S0022112009990644 Published online by Cambridge University Press

Thompson, J. F., Warsi, Z. U. A. & Mastin, C. W. 1995 *Numerical Grid Generation: Foundations and Applications*. North Holland.

Timoshin, S. N. 1997 Instabilities in a high-Reynolds-number boundary layer on a film-coated surface. *J. Fluid Mech.* **353**, 163–195.

Tsao, J. C., Rothmayer, A. P. & Ruban, A. 1997 Stability of air flow past thin liquid films on airfoils. *Comput. Fluids* **26** (5), 427–452.

Tsiglifis, K. & Pelekasis, N. A. 2005 Nonlinear oscillations and collapse of elongated bubbles subject to weak viscous effects. *Phys. Fluids* **17**, 102101.

Tutty, O. R. & Cowley, S. J. 1986 On the stability and the numerical simulation of the unsteady interactive boundary-layer equation. *J. Fluid Mech.* **168**, 431–456.

Veldman, A. E. P. 1981 New quasi-simultaneous method to calculate interacting boundary layers. *AIAA J.* **19**, 79–85.

Yih, C. S. 1990 Wave formation on a liquid layer for de-icing airplane wings. *J. Fluid Mech.* **212**, 41.

https://doi.org/10.1017/S0022112009990644 Published online by Cambridge University Press